JGR Oceans

RESEARCH ARTICLE
10.1029/2018JC014453

Global Estimates of the Energy Transfer From the Wind to the Ocean, With Emphasis on Near-Inertial Oscillations

M. Mar Flexas[1], Andrew F. Thompson[1], Hector S. Torres[2], Patrice Klein[2], J. Thomas Farrar[3], Hong Zhang[2,4], and Dimitris Menemenlis[2]

[1]Environmental Science and Engineering, California Institute of Technology, Pasadena, CA, USA, [2]Jet Propulsion Laboratory, California Institte of Technology, Pasadena, CA, USA, [3]Department of Physical Oceanography, Woods Hole Oceanographic Institution, Woods Hole, MA, USA, [4]Joint Institute for Regional Earth System Science and Engineering, University of California, Los Angeles, CA, USA

Key Points:
- Surface kinetic energy fluxes from LLC simulations lead to 4.71 TW, this is 25–85% higher than previous global estimates
- There is positive contribution to wind power input (WPI) at large scale and near-inertial (NI) band, and negative WPI at mesoscale, tidal frequencies and IGWs
- Low WPI at NI band (0.16 TW) suggests that wind variability on scales <6 hr and <15 km are critical to better representing WPI in GCMs

Supporting Information:
- Supporting Information S1

Correspondence to:
M. M. Flexas,
marf@caltech.edu

Citation:
Flexas, M. M., Thompson, A. F., Torres, H. S., Klein, P., Farrar, J. T., Zhang, H., & Menemenlis, D. (2019). Global estimates of the energy transfer from the wind to the ocean, with emphasis on near-inertial oscillations. *Journal of Geophysical Research: Oceans*, *124*, 5723–5746. https://doi.org/10.1029/2018JC014453

Received 15 AUG 2018
Accepted 27 JUN 2019
Accepted article online 3 JUL 2019
Published online 15 AUG 2019

Abstract Estimates of the kinetic energy transfer from the wind to the ocean are often limited by the spatial and temporal resolution of surface currents and surface winds. Here we examine the wind work in a pair of global, very high-resolution (1/48° and 1/24°) MIT general circulation model simulations in Latitude-Longitude-polar Cap (LLC) configuration that provide hourly output at spatial resolutions of a few kilometers and include tidal forcing. A cospectrum analysis of wind stress and ocean surface currents shows positive contribution at large scales (>300 km) and near-inertial frequency and negative contribution from mesoscales, tidal frequencies, and internal gravity waves. Larger surface kinetic energy fluxes are in the Kuroshio in winter at large scales (40 mW/m^2) and mesoscales (−30 mW/m^2). The Kerguelen region is dominated by large scale (∼20 mW/m^2), followed by inertial oscillations in summer (13 mW/m^2) and mesoscale in winter (−12 mW/m^2). Kinetic energy fluxes from internal gravity waves (−0.1 to −9.9 mW/m^2) are generally stronger in summer. Surface kinetic energy fluxes in the LLC simulations are 4.71 TW, which is 25–85% higher than previous global estimates from coarser (1/6–1/10°) general ocean circulation models; this is likely due to improved representation of wind variability (6-hourly, 0.14°, operational European Center for Medium-Range Weather Forecasts). However, the low wind power input to the near-inertial frequency band obtained with LLC (0.16 TW) compared to global slab models suggests that wind variability on time scales less than 6 hr and spatial scales less than 15 km are critical to better representing the wind power input in ocean circulation models.

1. Introduction

The transport of energy within and between the atmosphere and ocean plays a major role in setting both regional and global characteristics of Earth's climate. The wind stress is, globally, a net source of kinetic energy that, converted into power input, supports the global overturning circulation as well as a deep stable stratification (Wunsch & Ferrari, 2004). The kinetic energy transfer from the wind to the ocean is dominated by the surface gravity wave field (Rascle et al., 2008). Huang (2004) determined the kinetic energy fluxes caused by wind into the surface ocean to be ∼64 TW, ∼60 TW (1 TW = 10^{12} W) of which cause surface waves (Wang & Huang, 2004). However, almost all the energy coming from the surface wave field is dissipated in the first 3 m of the ocean and/or on the beach, when surface waves break, and therefore, it has little impact on the ocean general circulation (Ferrari & Wunsch, 2009). Because of computational cost, global ocean circulation models cannot explicitly represent surface gravity waves, missing the potential contribution of Stokes transport and other upper ocean processes to the ocean general circulation through modifications of surface boundary layer transport (McWilliams & Restrepo, 1999).

Early estimates of kinetic energy fluxes caused by wind to the ocean relied principally on time-averaged observations of surface wind speed and geostrophic surface velocities obtained from satellite altimetry (Wunsch, 1998). These studies resulted in a canonical value of 1 TW of wind work that enters the geostrophic component of the ocean circulation (Ferrari & Wunsch, 2009). Subsequent studies have highlighted the complexities of making this calculation, as well as possible sources of error in wind work estimates. Energy input can vary substantially in both space and time as the wind work depends sensitively on atmospheric wind speeds, ocean surface velocities, and the relative orientation of these two properties (see equation (1)). Efforts to improve estimates of oceanic wind work have been extensive (e.g., Dawe & Thompson, 2006;

Duhaut & Straub, 2006; Hughes & Wilson, 2008; von Storch et al., 2007; Zhai, 2013; Zhai et al., 2012), yet there remain critical limitations in the spatial and temporal resolution of the available observations.

Calculation of power input into the ocean from surface winds requires both an estimate of the surface wind stress, which is typically represented using a bulk formula that involves atmospheric wind speeds at 10 m above the sea surface $\mathbf{U_{10}}$, and the ocean surface velocities $\mathbf{u}$. The surface wind stress $\boldsymbol{\tau}$, a vector quantity, is then given by

$$\boldsymbol{\tau} = \rho_{\text{air}} C_d \left|\mathbf{U_{10}} - \mathbf{u}\right| \left(\mathbf{U_{10}} - \mathbf{u}\right), \tag{1}$$

where ρ_{air} is the density of air at sea level and C_d is the drag coefficient (Large & Yeager, 2004). The time-mean kinetic energy transfer, F_s, between the atmosphere and the ocean is given by

$$F_s = \overline{\boldsymbol{\tau} \cdot \mathbf{u}} = \overline{\boldsymbol{\tau}} \cdot \overline{\mathbf{u}} + \overline{\boldsymbol{\tau}' \cdot \mathbf{u}'}, \tag{2}$$

where F_s has been divided into a time-mean component ($\bar{\cdot}$) and an eddy component using a Reynolds decomposition.

From (1), wind stress depends on the difference between wind and ocean velocities, which leads to a well-known source of kinetic energy flux reduction compared to stress assuming a resting ocean (Eden & Dietze, 2009). Previous studies show that accounting for the ocean-surface-velocity dependence of the wind stress leads to a basin-average reduction of power input by the wind of ~27% (Dawe & Thompson, 2006), of wind-induced near-inertial energy of approximately 40% and of wind power input into the near-inertial frequency band of approximately 20% (Rath et al., 2013). The importance of including ocean surface velocity in wind stress calculations used in estimating the wind work to surface currents has also been explored by Duhaut and Straub (2006), Hughes and Wilson (2008), and Wu et al. (2017) and shown to be of greatest importance in western boundary currents and in the Southern Ocean. Including surface velocity results in a weakened general ocean circulation and thus in a decreased northward global ocean heat transport (Wu et al., 2017). Hughes and Wilson (2008) note that previous calculations of wind work to the ocean employ smooth wind stress patterns associated with reanalysis products, which underestimate the power in wind stress at scales shorter than 500 to 1,000 km, as determined by comparison with scatterometer data (Milliff et al., 2004). The scale-dependence question, directly addressed in the works of Rimac et al. (2013) and Zhai (2017), is object of current studies. The impact of submesoscales, for instance, still remains unknown.

Storm track regions over oceanic western boundary currents and the Southern Ocean are regions with strong synoptic (1,000 km) wind variability, coupled with substantial mesoscale kinetic energy in the surface ocean. The impact of temporally varying winds on oceanic power input has been examined recently in a series of studies by Zhai et al. (2012), Zhai and Wunsch (2013), Zhai (2013), and Rimac et al. (2013). An analysis of wind stress calculations using monthly and 6-hourly winds, which are used to define a mean and eddy component, revealed that the total power input can increase by over 70% when synoptic winds are included (Zhai, 2013). Rimac et al. (2013) shows additional dependence of near-inertial band wind work on the time scale of the forcing for data sampling periods between 6 and 1 hr. Regions that make the greatest contribution to this eddy component exhibit strong mesoscale activity, such as western boundary currents and the Southern Ocean (Zhai, 2013). An open question that was not addressed in this study, which considered the wind work on the geostrophic flow, is the temporal and spatial scales that need to be measured to accurately resolve the eddy power input from the surface wind stress. Here we adopt a spectral approach to assess the distribution of power input from fluctuating winds over a range of frequencies.

The winds (see equation (2)) inject energy into geostrophic and ageostrophic motions, including surface waves. Among the ageostrophic motions, the near-inertial peak is an important reservoir of kinetic energy in the mixed layer. Propagation of near-inertial oscillations out of the mixed layer into the deep ocean is a key source of internal wave energy, comparable to the energy from internal tides (MacKinnon et al., 2010; Wunsch & Ferrari, 2004), and it has been postulated as a primary source of energy for driving the global overturning circulation. However, other works state this quantity is not very large due to turbulent mixing, by which a substantial part of the wind energy input is dissipated in the mixed layer (Zhai et al., 2009). Assuming that the amplitude of inertial currents, $|\mathbf{u_I}|$, is vertically uniform in the mixed layer, the inertial horizontal kinetic energy in the mixed layer (KE_I) can be defined as

$$KE_I = \frac{1}{2}\rho H \left|\mathbf{u_I}\right|^2, \tag{3}$$

where ρ is the seawater density in the mixed layer of depth H. A monthly climatological global census of near-inertial energy derived from surface drifter observations (Chaigneau et al., 2008) has revealed significant discrepancies in energy content with frequently used mixed layer models (Alford, 2001). This discrepancy is attributed to a lack of resolution of the mesoscale field in numerical models (Chaigneau et al., 2008). Differences are particularly evident in the Southern Ocean, which has the largest mixed layer energy content (Chaigneau et al., 2008) but is a region where measurements are sparse. To explore the contribution to global mixed layer energy due to inertial motions and its distribution throughout the ocean, we estimate the near-inertial horizontal kinetic energy in the mixed layer. Then, we decompose the sources and sinks of the horizontal kinetic energy balance of near-inertial currents in the mixed layer.

To realize these objectives, we make use of a global, very high-resolution MIT general circulation model (MITgcm) product that provides hourly output at spatial resolutions of a few kilometers and includes tidal forcing. One of the most useful aspects of this simulation is that it accurately represents physical processes down to the scale of 5–10 km, thus including at least crude representations of most physical mechanisms that contribute to ageostrophic motions, outside of surface waves. The model also captures the physical processes that are responsible for variability in mixed layer depths (hereafter MLDs) at periods shorter than the seasonal shoaling and deepening cycle, for example, mixed layer baroclinic instability (Fox-Kemper et al., 2008). Another unique feature of this simulation is that it provides hourly output of full three-dimensional model prognostic variables, making it a remarkable tool for the study of ocean and air-sea exchange processes.

2. Data and Methods

2.1. MITgcm Ocean Simulation

We use a high-resolution ocean simulation based on a Latitude-Longitude-polar Cap (hereafter LLC) configuration of the MITgcm (Hill et al., 2007; Marshall et al., 1997). We use two LLC configurations here, one with nominal 1/48° grid resolution and one with nominal 1/24° grid resolution. This simulation provides hourly output of full three-dimensional model prognostic variables. At present, LLC 1/24° output is available from April 2011 to March 2013, while LLC 1/48° output is available from September 2011 to November 2012. In this contribution we use 1 year of data, from 15 November 2011 to 14 November 2012, from each configuration. Although a single year is not of sufficient duration to be representative of the mean ocean state, it can provide useful information on upper ocean variability up to seasonal scale.

The LLC 1/48° (1/24°) grid has 13 square tiles with 4,320 (2,160) grid points on each side and 90 vertical levels. Horizontal grid spacing ranges from 0.75 (1.5) km near Antarctica to 2.2 (4.4) km at the equator, and vertical levels have 1-m thickness near surface to better resolve the diurnal cycle. The model configuration includes a flux-limited, seventh-order, monotonicity-preserving advection scheme (Daru & Tenaud, 2004) and the modified Leith scheme of Fox-Kemper and Menemenlis (2008) for horizontal viscosity. Vertical viscosity and diffusivity are parameterized according to the K-profile parameterization (Large et al., 1994). Bottom drag is quadratic (drag coefficient, $C_d = 0.0021$), and side drag is free slip. Partial cells (Adcroft et al., 1997) are used to represent the sloping sea floor in our z-level vertical discretization. Bathymetry is from ETOPO-5 (1988).

The simulation is initialized from a data-constrained global ocean and sea ice solution provided by the Estimating the Circulation and Climate of the Ocean, Phase II (ECCO2) project (Losch et al., 2010; Menemenlis et al., 2008). Configuration details are similar to those previously used by the ECCO2 project except that the LLC simulation includes atmospheric pressure and tidal forcing. LLC simulations carry the full luni-solar tidal potential. This is, after Arbic et al. (2010), the second global, general ocean circulation model (GCM) that includes tidal forcing. These simulations have the potential to simulate SSH variance on a global scale (Savage, Arbic, Alford, et al., 2017; Savage, Arbic, Richman, et al., 2017) and carry a partial internal gravity wave (IGW) continuum (Rocha, Chereskin, et al., 2016; Rocha, Gille, et al., 2016). In the 0.2- to 1-cpd band, both HYCOM and MITgcm are generally deficient relative to observations, for reasons not yet understood (Arbic et al., 2018). The supertidal IGW continuum is captured better in MITgcm simulations, due to their higher horizontal and vertical resolution with respect to HYCOM simulations (Arbic et al., 2018; Savage, Arbic, Alford, et al., 2017).

Surface boundary conditions are from 6-hourly output from the 0.14° (~15 km) European Center for Medium-Range Weather Forecasts (ECMWF) atmospheric operational model analysis (European Centre for Medium-Range Weather Forecasts, 2011). The 6-hourly atmospheric fields are linearly interpolated in

time. The model simulation uses the Large and Pond (1982) bulk formulae for converting atmospheric conditions to ocean surface stress over open ocean. The ocean surface stress accounts for the velocity of wind and ocean currents (equation (1)).

The 6-hourly wind forcing is a serious limitation of the model. In a recent (unpublished) study on the impact of using high-frequency atmospheric boundary conditions on ocean model solutions, the ECCO team used a global configuration of the MITgcm, the so-called LLC270 configuration (the ECCO v5 workhorse) that has ~24-km horizontal grid spacing, to simulate ocean circulation using ERA5 (Copernicus Climate Change Service (C3S), 2017) and its derived products as atmospheric forcing. The authors conducted two simulations, one forced with 1-hourly ERA5 fields and one forced with 6-hourly ERA5-derived fields, and calculated the power spectral density of 1-hourly surface current speed from the two simulations at several latitudes. The hourly forcing results in a near-inertial peak that is 2–3 times higher than that generated by the 6-hourly forcing—the higher the latitude, the larger the difference—and has more variability at a wide frequency band centered around the inertial frequency. Future LLC simulations will use the new generation of ECMWF atmospheric reanalysis (Copernicus Climate Change Service (C3S), 2017).

The model does not include representation of surface waves and therefore ignores the nonlinear generation of near-inertial oscillations by high-frequency gravity waves (Hasselmann, 1970). The model also fails to represent the Stokes drift and the potential contribution of the Stokes transport to the ocean general circulation through modifications of surface boundary layer transport (McWilliams & Restrepo, 1999). Additional caveats of the model regarding the representation of near-inertial waves may involve the complicated meridional structure of near-inertial waves, in which the vertical and zonal wavenumbers account for slight spectral peak displacements above the inertial frequency, peak width, and spatial coherence of near-inertial waves (not investigated here; Fu, 1981; Kundu, 1976; Munk & Phillips, 1968) .

2.2. Methods

2.2.1. Surface Kinetic Energy Flux

The kinetic energy flux from the wind into the surface ocean is estimated as the dot product of surface wind stress and ocean surface currents (2). An efficient method for assessing contributions to the wind power input across a range of frequencies and wavenumbers is to calculate the surface kinetic energy flux using a spectral approach. We calculate the frequency (ω)-wavenumber (k) cospectrum of wind stress and ocean surface currents, $\Lambda_{\boldsymbol{\tau u}}$, as

$$\Lambda_{\boldsymbol{\tau u}}(k,\omega) = Re[\hat{\boldsymbol{\tau}} \cdot \hat{\mathbf{u}}^*], \tag{4}$$

where $\hat{\boldsymbol{\tau}}$ is the Fourier transform of the wind stress vector and $\hat{\mathbf{u}}^*$ is the conjugate of the Fourier transform of the surface currents vector. Before computing the frequency-wavenumber cospectrum, the mean and the linear trend in space and time were removed, and the data set was multiplied by a three-dimensional (x, y, and t) Hanning window. The cospectrum was calculated in 15° latitude × 15° longitude boxes and 3-month hourly output. This permits to resolve wavelengths from ~4 to ~750 km and periods from 2 hr to 45 days. The cospectrum was azimuthally integrated in wavenumber space in order to express the cospectrum in terms of wavenumber magnitude.

We calculate $\Lambda_{\boldsymbol{\tau u}}$ (equation (4)) in three target regions with distinct ocean dynamics: the Indian sector of the Antarctic Circumpolar Current (ACC), where there are large temporal and spatial changes in MLD; the Kuroshio current, where kinetic energy fluxes are the most intense; and the northeast Atlantic, in a relatively low eddy kinetic energy region near the boundary between the subtropical and subpolar gyres. This last region, while not a peak site of kinetic energy, is still frequented by mesoscale eddies. Stirring by these eddies can lead to significant submesoscale frontal development, as recently determined by the year-long OSMOSIS field program (Thompson et al., 2016).

2.2.2. Near-Inertial Kinetic Energy Budget

To estimate near-inertial currents, we use a Hamming window to design a band-pass filter that removes frequencies outside the $0.8f/2\pi < \omega < 1.2f/2\pi$ band, where f is the inertial frequency at a given latitude. We mask the equatorial band, between 5° N and 5° S, where f tends to zero. We filter the wind stress at near-inertial frequencies using the same filter we used for ocean currents.

We estimate the near-inertial horizontal kinetic energy in the mixed layer assuming that the amplitude of inertial currents is vertically uniform in the mixed layer (3). The MLD used in this work is the boundary

layer depth as determined from the simulation's K-profile parameterization scheme (Large et al., 1994), but our results would not be qualitatively changed by using a different MLD definition. We performed a regional analysis in the northeast Atlantic comparing MLD estimated from in situ data from Thompson et al. (2016) to model boundary layer depth and to model MLD. We should note that in situ MLD data and model MLD are not from the same year (so did not experience the same forcing). We calculated in situ MLD and model MLD using the criteria of a potential density difference of 0.03 kg m^3 (De Boyer Montegut et al., 2004; Dong et al., 2008). We found that discrepancies between these three quantities (in situ MLD, model MLD, and model boundary layer depth) varied seasonally, with smaller discrepancies in summer and larger discrepancies during winter months, likely related to having less variability in summer than in winter. Average values of in situ MLD were 20 ± 7 m in summer and 185 ± 75 m in winter. We found that boundary layer depth underestimated observed MLD by less than 25% in winter and by less than 15% in summer. In turn, model MLD overestimated observed MLD by more than 50% in winter and by 10% in summer. The (upper-bound) error induced by the underestimation of observed MLD in (3) is estimated to be less than 25% in annual integrations.

We estimate the KE_I budget in the mixed layer as (Majumder et al., 2015)

$$\frac{\mathrm{d}(KE_I)}{\mathrm{dt}} = \Pi_W + \Pi_H + \Pi_R, \tag{5}$$

where Π_W is the kinetic energy flux from the wind transferring energy to near-inertial currents in the mixed layer, calculated as

$$\Pi_W = \boldsymbol{\tau_I} \cdot \mathbf{u_I}, \tag{6}$$

with $\boldsymbol{\tau_I}$ the wind stress filtered at the inertial band, Π_H is the kinetic energy flux due to change in MLD, given by

$$\Pi_H = \frac{1}{2}\rho|\mathbf{u_I}|^2\frac{\mathrm{d}H}{\mathrm{dt}}, \tag{7}$$

and Π_R accounts for all other processes that add or remove energy from the mixed layer, including advection, dissipation, and radiation losses. We calculate Π_W, Π_H, and $\mathrm{d}KE_I/\mathrm{dt}$ and calculate Π_R as a residual flux from (5).

The quantities KE_I, Π_W, Π_H, and Π_R are calculated from hourly fields of wind stress, surface currents, and MLD. To obtain annual-average maps, the resulting fields are time-averaged over one annual cycle (from 15 November 2011 to 14 November 2012). Seasonal maps are obtained from averaging over 3-month periods, defined as follows. For JFM, we average from 1 January 2012 to 31 March 2012; for AMJ, from 1 April 2012 to 30 June 2012; for JAS, from 1 July 2012 to 30 September 2012; and for OND, from 1 October 2012 to 14 November 2012 and 15 December 2011 to 31 December 2011.

For the sake of computational efficiency, the analyses are applied to horizontal grid points separated by 1° of latitude and longitude. To ensure that this "skipping method" does not include substantial error, the total surface kinetic energy flux was calculated on the original grid and on the subsampled grid over the North Atlantic domain. The error induced by the skipping method was smaller than 1%.

3. Results

3.1. Surface Kinetic Energy Fluxes

The total wind energy input is calculated following (2) (Figure 1). Global estimates from hourly output are 4.71 TW (1 TW = 10^{12} W) for LLC 1/48° and 4.79 TW for LLC 1/24° (Table 1). From November to January, the contribution from the Northern (Southern) Hemisphere to the global kinetic energy flux is ~2 TW (~3 TW). From March to October, their respective contributions are ~1 TW for the Northern Hemisphere and ~4 TW for the Southern Hemisphere.

The cospectrum of wind stress and ocean surface currents (Figure 2; for reference, the cospectrum in linear form is shown in supporting information Figure S1) permits an investigation of the scales at which surface kinetic energy flux is a source or sink of energy to the surface ocean. There is positive contribution to surface kinetic energy fluxes, that is, transfer of energy from the atmosphere to the ocean, at large spatial and temporal scales (>100 km, 10 hr to 4 days), negative contribution from mesoscales (30–300 km at subinertial

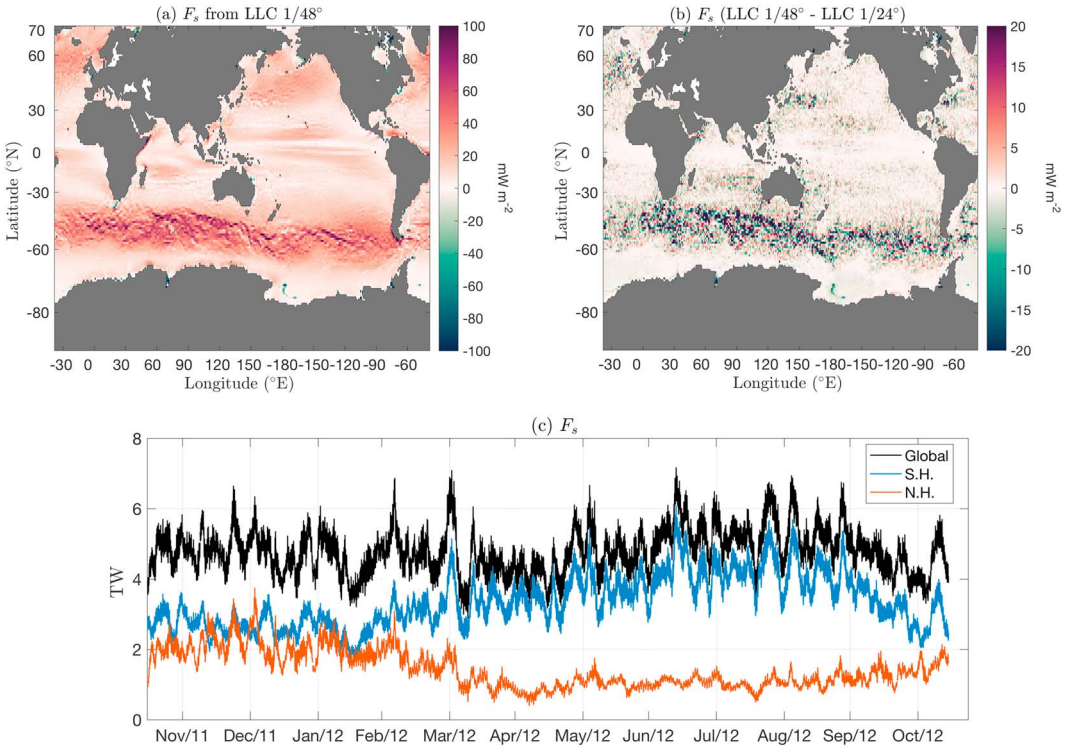

Figure 1. Surface kinetic energy fluxes computed from hourly wind stress and surface ocean currents (equation (2)). (a) Annual mean from LLC 1/48°. (b) Difference of LLC 1/48°-LLC 1/24°. (c) Global mean (black) and average over the Northern (N.H.) and Southern (S.H.) Hemispheres from LLC 1/48. LLC = Latitude-Longitude-polar Cap.

frequencies), and negative contribution from tides, in particular for semidiurnals, at these specific locations. This loss of energy from the ocean to the atmosphere at mesoscale arises from the surface wind flux formulation when surface ocean currents are included in the calculation of wind stress (Eden & Dietze, 2009; see Appendix A). This can be explained by the asymmetric response of the dot product of wind stress and surface currents along the sides of an eddy when surface ocean currents are considered in the calculation of wind stress. When the wind and the surface current are moving in the same direction, the resulting stress (equation (1)) is positive but relatively small. In turn, when the wind and the surface current are moving in opposite direction, the stress is large and negative. Such asymmetry leads to a net effect that, when integrated spatially, takes energy out of the eddy (Zhai et al., 2012) and results in a net negative wind energy input in the mesoscale and submesoscale regime (Figure 2).

In terms of regional differences among the three target areas, the largest seasonality is found in the North Pacific (Figures 2a and 2b). The North Atlantic shows, as expected from a relatively quiescent region, very small surface kinetic energy fluxes (Figures 2c and 2d). Finally, surface kinetic energy fluxes at the Southern Ocean mesoscale are characterized by larger wavelengths and longer periods than the Northern Hemisphere counterparts, in particular in winter time (Figures 2e and 2f).

Table 1
Surface Kinetic Energy Flux Estimates Using Hourly, Daily Averaged, 3-Day Averaged, and 7-Day Averaged Fields From Latitude-Longitude-Polar Cap 1/48°

Averaging	Total flux (TW)	Near-inertial flux (TW)
1-hr	4.71 (4.79)	0.16 (0.17)
1-day	4.22	0.11
3-day	3.43	0.09
7-day	2.90	0.08

*Note.*Estimates from Latitude-Longitude-polar Cap 1/24° are in parentheses.

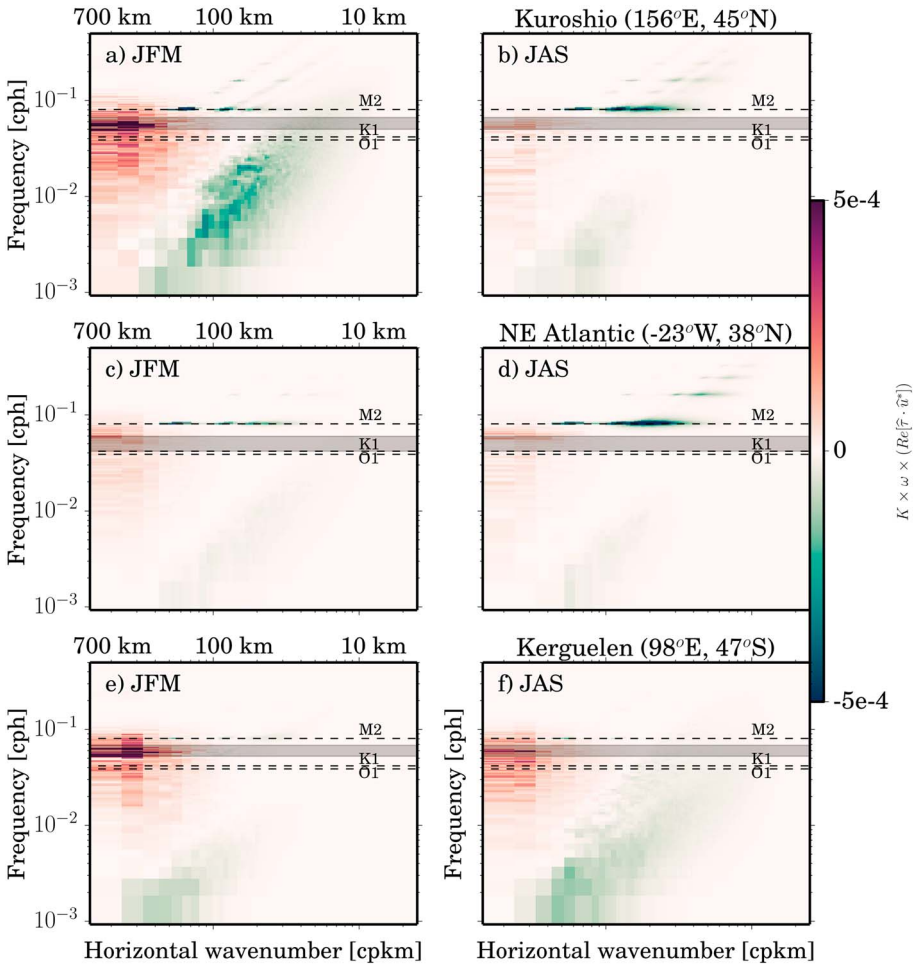

Figure 2. Frequency-wavenumber cospectrum of wind stress and ocean surface currents (in W/m^2) in three target regions in JFM and JAS months. The three target regions are (a,b) the Kuroshio Extension [31–46° N, 156–176° W], (c,d) NE Atlantic [38–53° N, 23° W–8° E], and (e,f) Southern Ocean, east of Kerguelen Plateau [32–47° S, 98–113° E]. To better highlight the variance in the spectral space, the cospectrum is multiplied by the wavenumber, k, and frequency, ω.

The cospectrum permits to quantify the relative contribution of each dynamic regime (Figure 3 and Table 2). In this analysis we consider broad definitions of large scale (lengthscales, L > 300 km; periods T > 1.25f), mesoscale (300 km > L > 30 km; periods T > 1.25f), and submesoscale (L < 30 km; periods T > 1.25f). We consider the semidiurnal band from 12.66 to 11.97 hr for all wavenumbers. The inertial band spans over all the inertial periods included in the domain (which may lead to overestimation) for all wavenumbers. The IGW is the continuum between normal mode 1 and normal mode 10 (the highest normal mode allowed by the horizontal resolution of the numerical model), for periods T < 12.66 hr. See Appendix B for Root-Mean-Square (RMS) error estimation.

The largest surface kinetic energy fluxes are found in the North Pacific (Kuroshio) in JFM at large scales (40 mW/m^2) followed by mesoscales (−30 mW/m^2) (Table 2). The Kerguelen region is dominated by large scale (∼20 mW/m^2 in JFW and JAS), followed by inertial oscillations in JFM (13 mW/m^2) and mesoscale in JAS (−12 mW/m^2). The North Atlantic shows relatively low energy fluxes (<10 mW/m^2).

The relative contribution of IGW to total wind power input varies among regions and seasons 2. In the Kuroshio, in winter, the contribution of IGW (−5 ±1 mW/m^2) to total wind power input is small with respect to the contribution of mesoscale (−29 ± 4 mW/m^2) and large scale (39 ± 5 mW/m^2) processes. In summer, instead, large scales (7 ± 1 mW/m^2), mesoscales (−4 ± 1 mW/m^2), and IGW (−7 ± 1 mW/m^2) are all within similar range. In the NE Atlantic, surface kinetic energy fluxes at large scales, mesoscales, and IGW have similar magnitude (9, −3, and −2 mW/m^2, respectively, in winter). In the Kerguelen region, IGWs are small

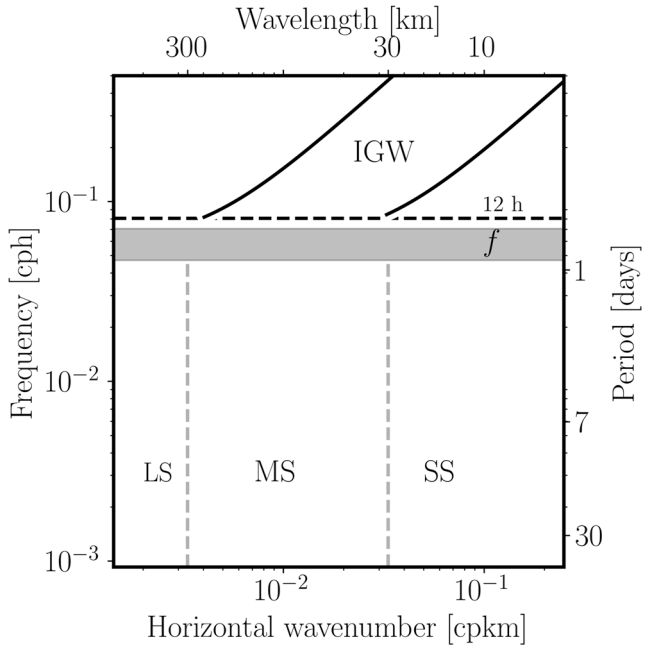

Figure 3. Schematic of the wavenumber/frequency regimes considered in this study. The large scale (LS) contains lengthscales, L > 300 km and periods T > 1.25*f*. The mesoscale (MS) is defined by 300 km > L > 30 km and periods T > 1.25*f*. The submesoscale (SS) has L < 30 km and periods T > 1.25*f*. The semidiurnal band (12 hr) includes periods from 12.66 to 11.97 hr and all wavenumbers. The inertial band (*f*) spans over all the inertial periods included in the domain (which may lead to overestimation) and all wavenumbers. The internal gravity wave field (IGW) is the continuum between normal mode 1 and normal mode 10 (the highest normal mode allowed by the horizontal resolution of the numerical model), for periods T < 12.66 hr.

(<1 mW/m^2). To our knowledge, this is the first time that the impact of IGWs on the surface kinetic energy fluxes has been documented.

Figure 4 shows the contribution of the time-mean (obtained from the annual-mean fields of wind stress and surface currents) and time-varying winds and currents to the total surface kinetic energy fluxes (Figure 1a). Time-mean fluxes are larger in the Southern Ocean and in the equatorial region. Time-varying fluxes show larger values at latitudes greater than 30° and little spatial structure. Using daily averaged fields in surface kinetic energy flux calculations reduces their values by 10%, while using 7-day averaged wind stress and surface velocity fields reduces surface kinetic energy fluxes by 40% (Figure 5a and Table 1). These reductions are consistent with previous studies (Rimac et al., 2013).

Table 2
Contribution of Large Scale, Mesoscale, Submesoscale, and Internal Gravity Waves to Surface Kinetic Energy Flux Estimates (in mW/m^2) From Latitude-Longitude-Polar Cap 1/48° Output With Root-Mean-Square Error for Kuroshio Region, NE Atlantic, and Kerguelen for JFM and JAS months

	Kuroshio		NE Atlantic		Kerguelen	
	JFM	JAS	JFM	JAS	JFM	JAS
Large scale	39.3 ± 5.1	7.4 ± 0.9	9.3	6.0	21.7	18.6
Mesoscale	−28.7 ± 3.7	−3.7 ± 0.5	−3.2	−1.5	−0.9	−12.2
Submesoscale	−7.2 ± 0.9	−0.2 ± 0.0	−1.6	−0.2	−0.4	−4.6
Inertial	13.5 ± 1.8	1.8 ± 0.2	3.2	2.1	13.3	6.1
Semidiurnals	0.0 ± 0.0	−5.3 ± 0.7	−1.5	−8.2	4.1	2.2
IGW	−5.3 ± 0.7	−7.1 ± 0.9	−2.3	−9.9	−0.1	−0.9
Total	−4.8 ± 0.6	−6.7 ± 0.9	3.9	−6.4	15.2	9.8

Note. See Figure 3 for the definition of these different regimes in wavenumber/frequency domain. See Appendix B for Root-Mean-Square error estimation.

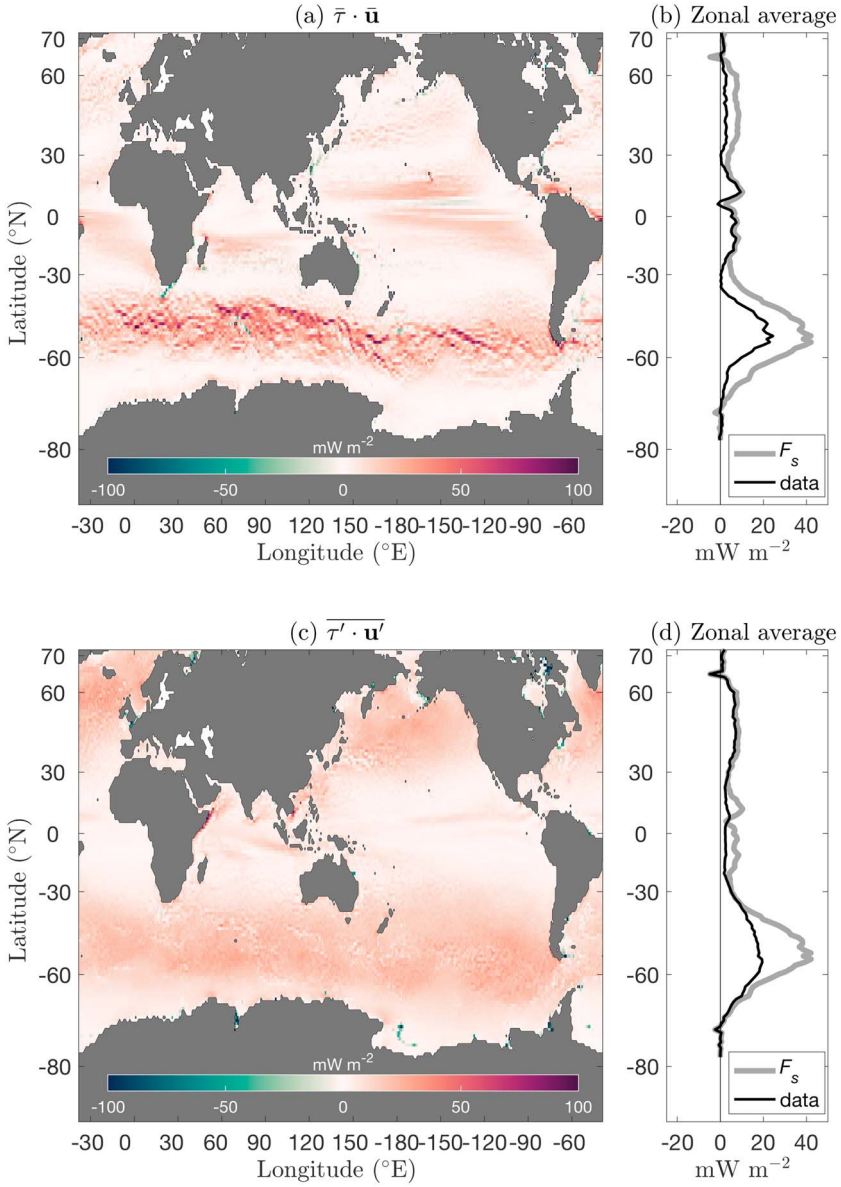

Figure 4. Spatial distributions of (a,b) time-mean fluxes, $\bar{\boldsymbol{\tau}} \cdot \bar{\mathbf{u}}$, and (c,d) eddy fluxes, $\overline{\boldsymbol{\tau}' \cdot \mathbf{u}'}$ from LLC 1/48°. Surface kinetic energy fluxes (F_s) have been divided into a time-mean component ($\bar{\cdot}$) and an eddy component using a Reynolds decomposition, where $F_s = \overline{\boldsymbol{\tau} \cdot \mathbf{u}} = \bar{\boldsymbol{\tau}} \cdot \bar{\mathbf{u}} + \overline{\boldsymbol{\tau}' \cdot \mathbf{u}'}$. (b) and (d) are the respective zonal averages of (a) and (c), "data" presented in black. For comparative purposes, the zonal average of total wind energy input is also shown, F_s presented in gray.

The kinetic energy flux contribution at near-inertial frequencies is a source of energy to the ocean; this is consistent with earlier studies from drifter data and numerical models (e.g., Elipot & Gille, 2009; Rimac et al., 2013). Kinetic energy fluxes at the near-inertial band (Figure 6) are 2 orders of magnitude smaller than total kinetic energy fluxes (Figure 1). In general, major current systems show annual averages of 2 mW/m^2, with maximum annual-mean fluxes at the near-inertial band found as a reflection of storm tracks in the Kuroshio region (4 mW/m^2). These values are consistent with those obtained using drifter data (Elipot & Gille, 2009). Using a spectral approach, Elipot and Gille (2009) estimated total fluxes in the Southern Ocean of about 40 mW/m^2 and of 2 mW/m^2 at the near-inertial band; these values are similar to our LLC estimates (Figures 1a, 5a, and 6). Elipot and Gille (2009) considered these values to be underestimated due to the lack of temporal variability in the wind reanalysis product used (the 6-hourly ECMWF ERA-40 product, with spatial resolution of 1.125° by 1.125°; Simmons & Gibson, 2000) and in the drifter product (Chaigneau et al.,

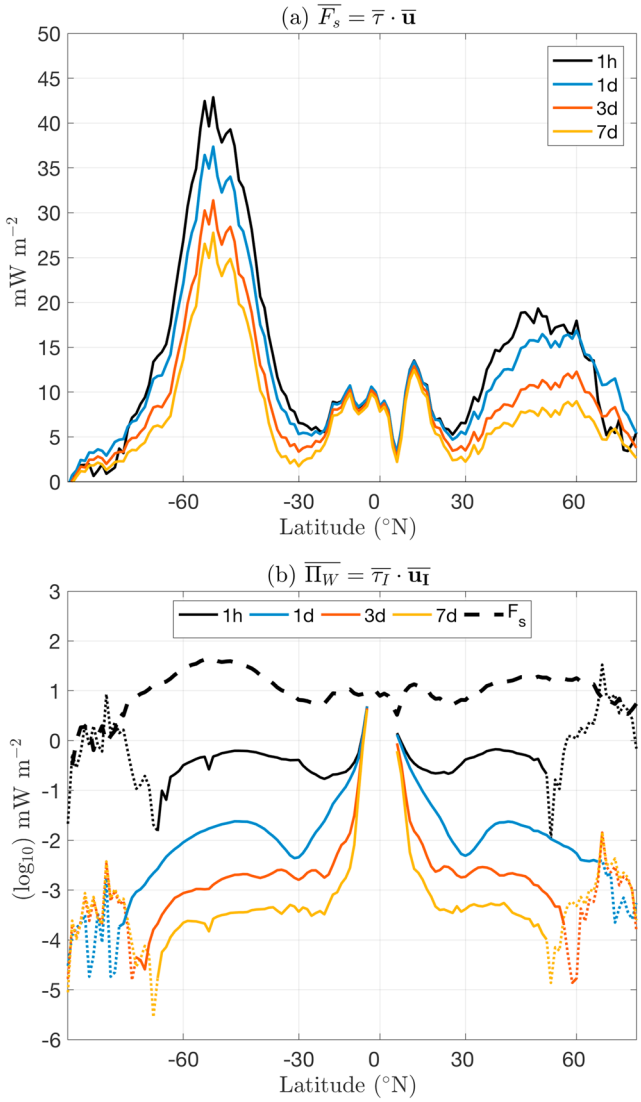

Figure 5. Impact of temporally averaging wind stress and surface currents (denoted with overline bars) on surface kinetic energy fluxes. Colors denote the averaging windows applied to each variable. (a) Zonal averages of surface kinetic energy fluxes from hourly mean (black), daily-mean (blue), 3-day mean (orange), and 7-day mean (yellow) variables. (b) Same as (a), for the near-inertial band. For reference, hourly mean total surface kinetic energy fluxes are shown (thick broken black line). Note the logarithmic scale in (b). Dotted lines indicate negative logarithmic values of Π_W (under ice).

2008; Elipot & Lumpkin, 2008). Future efforts should consider applying the new global product of regular hourly drifter locations and velocities derived by Elipot et al. (2016), although the lack of wind variability in atmospheric reanalysis remains an issue (Gille, 2005).

Stronger kinetic energy fluxes in LLC are observed in winter and autumn months in each hemisphere, although the seasonality and spatial variability of surface kinetic energy fluxes is larger in the Northern Hemisphere. In the Southern Hemisphere, fluxes appear evenly distributed over the Southern Ocean. There are, however, regions where surface kinetic energy fluxes at the near-inertial band show annual-mean negative values. These include regions poleward of 60° latitude, where sea ice is present over part of the year, and marginal seas like the North Sea (North Atlantic), the Coral Sea (South Pacific), and waters over the Falkland/Malvinas Plateau (South Atlantic). In terms of zonal and meridional components of surface kinetic energy fluxes at the near-inertial band, fluxes associated with meridional winds are larger in the Southern Ocean and in the subtropical and subpolar gyres, while zonal winds are more important close to the equator (not shown).

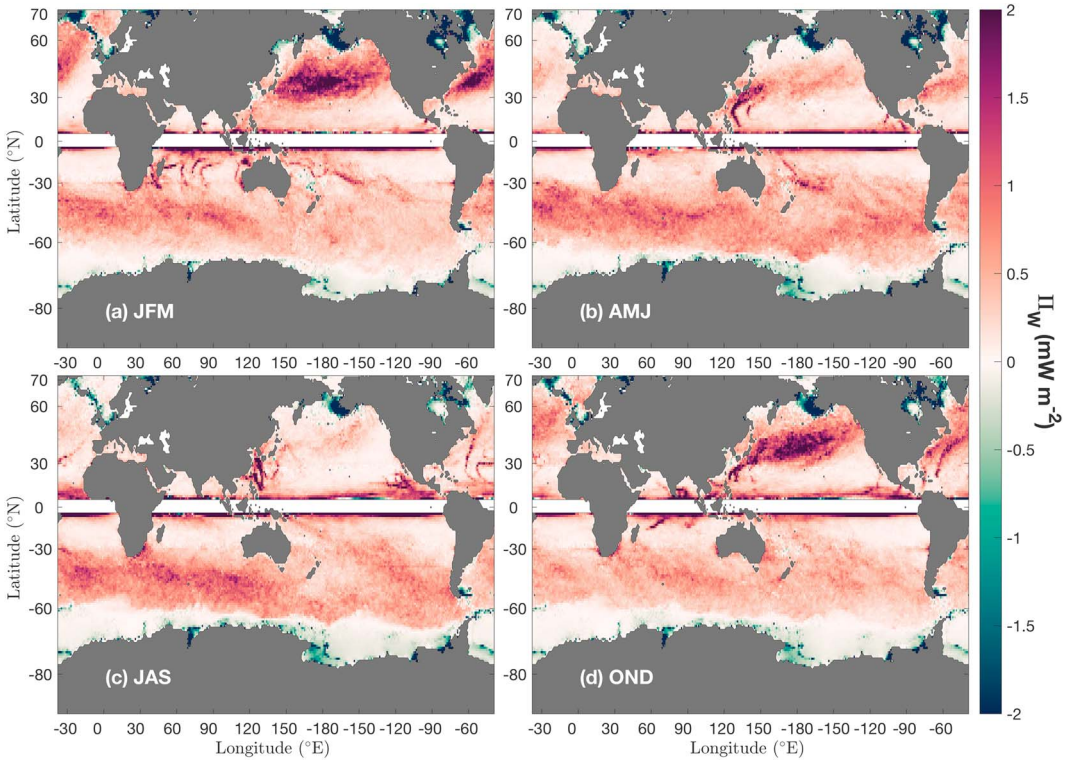

Figure 6. Seasonal (3-month averaged for (a) JFM, (b) AMJ, (c) JAS, and (d) OND months) maps of surface kinetic energy flux at near-inertial band (Π_W, in mW/m^2) calculated from hourly wind stress and ocean currents, both filtered at the near-inertial band.

Global surface kinetic energy fluxes in the near-inertial band are 0.16 TW in LLC 1/48° and 0.17 TW in LLC 1/24° (Table 1). However, this quantity is largely dominated by the contribution at the near-equatorial band (from 5° to 10° of latitude; data <5° latitude are not considered). Near-inertial currents are filtered out when using wind stress and surface currents fields that have been averaged over more than 1 day (Figure 5b).

Increasing model resolution reduces both total surface kinetic energy fluxes and energy fluxes at the near-inertial band. This could be explained by the fact that currents and winds are more uncorrelated with increasing horizontal resolution. However, the reduction in surface kinetic energy fluxes in the 1/48° model is too small to justify any firm conclusion (Table 1).

3.2. Near-Inertial Energy Content in the Mixed Layer

Kinetic energy at near-inertial frequencies in LLC, averaged over one year, represents 10% of total surface kinetic energy in the global ocean (Figure 7). The contribution of near-inertial kinetic energy to total kinetic energy varies regionally, from <10% in the Southern Ocean to ~25% in less energetic areas, like central areas of the Northern and Southern Pacific Ocean. At latitudes close to 30° N, the inertial frequency band includes diurnal tides. Maps of seasonally averaged surface inertial currents show distinct branches of the Kuroshio Extension in the Northern Pacific and reflect the distribution of the atmospheric storm tracks (Figure S2), with maximum eastward extension in winter and autumn (JFM and OND). In the Southern Hemisphere, surface inertial currents are strongest within a 30° latitude band, from ~15° S and ~45° S; their magnitude is larger in austral spring and summer (OND and JFM). Relatively strong inertial currents are observed in Drake Passage and off the western Antarctic Peninsula. Mean values of near-inertial currents in LLC are up to 10 cm/s in the North Pacific and up to 7 cm/s in the ACC (Figure S2).

The maximum inertial horizontal kinetic energy in the mixed layer (KE_I) is found between 30° S and 60° S (Figure 8). Long zonal bands of high kinetic energy ($KE_I \sim 600$ J/m^2) shift southward, from 30° S to 60° S, across each sector (Pacific, Indian, and Atlantic) of the ACC. Kinetic energy in the mixed layer due to near-inertial currents is larger, in both hemispheres, in their respective autumn and winter periods ($KE_I >$ 300 J/m^2). This pattern is especially clear in the North Pacific and in the Southern Ocean.

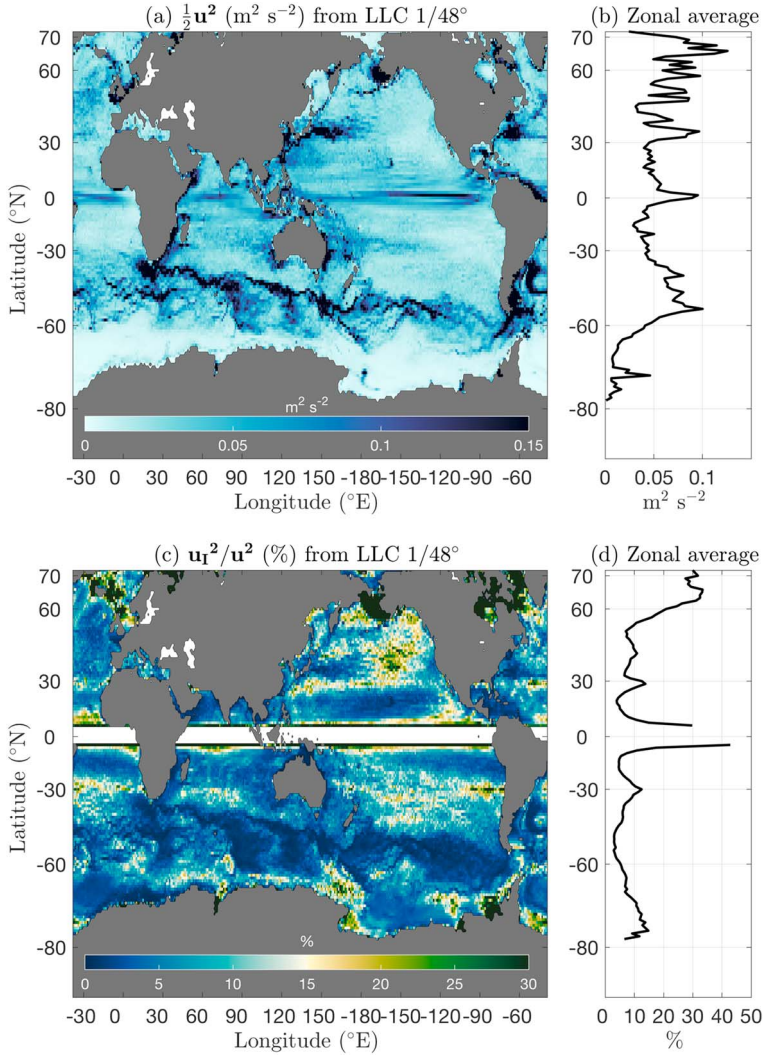

Figure 7. (a, b) Annual-average maps of surface kinetic energy from LLC 1/48° and its zonal average. (c, d) Contribution (in %) of surface kinetic energy at the inertial band to total kinetic energy. LLC = Latitude-Longitude-polar Cap.

In terms of differences in model output resolutions (1/48° vs. 1/24°), KE_I shows patterns that are a combination of differences in surface inertial currents and in MLD (Figure 9). Increasing the model resolution leads, globally, to larger inertial currents, reduced MLDs, and higher near-inertial kinetic energy in the mixed layer.

Comparing the LLC results with estimates obtained from surface drifters by Chaigneau et al. (2008), the magnitude of surface inertial currents in the model is underestimated by a factor of 2 throughout the ocean. For example, Chaigneau et al. (2008) reported mean values of near-inertial currents of up to 20 cm/s in the Kuroshio and North Pacific and up to 12 cm/s in the ACC; these values represent a loss of about 40–50% in LLC with respect to the observed values (Figure S2). In turn, the near-inertial energy in the mixed layer is underestimated in the LLC output by a factor of 2 to 5 with respect to estimates obtained from near-surface drifters from Chaigneau et al. (2008). Such underestimation is in agreement with previous numerical regional circulation model estimates (Dippe et al., 2015; Rath et al., 2014) and will be discussed in section 4.2.2.

3.3. Near-Inertial Kinetic Energy Budget in the Mixed Layer

The near-inertial kinetic energy budget in the mixed layer is estimated according to (5). To investigate the temporal evolution of each budget term, we examine an area East of the Kerguelen Islands (43° S, 93° E), a region of large EKE where the MLD experiences large variability. Following Majumder et al. (2015), a 7-day

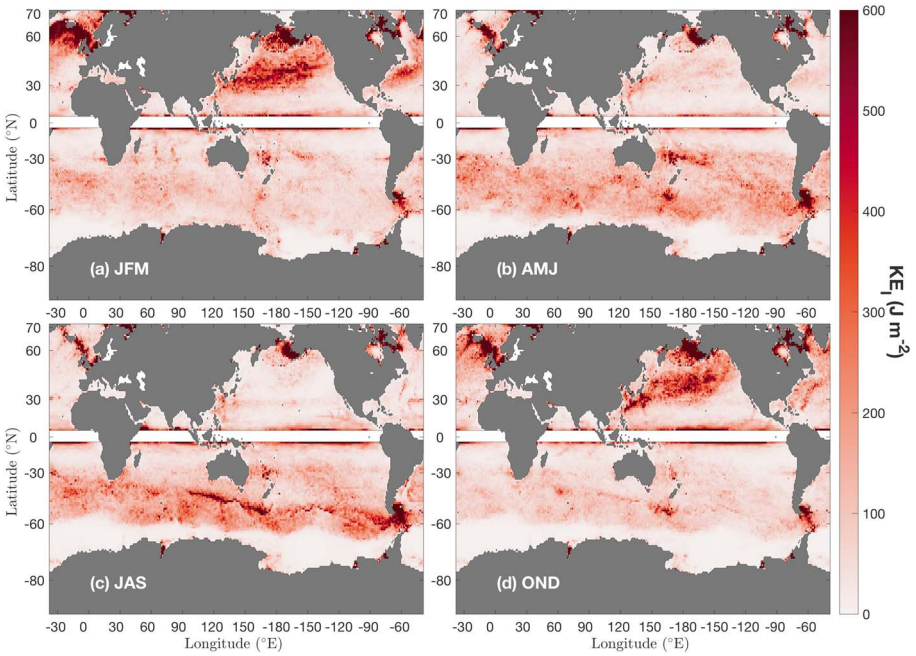

Figure 8. Seasonal (3-month averaged for (a) JFM, (b) AMJ, (c) JAS, and (d) OND months) maps of inertial horizontal kinetic energy (KE_I, in J/m^2) in the mixed layer.

running mean is used to filter out higher-frequency variability in the MLD (Figure 10a). After filtering, the rate of change in MLD is close to zero (Figure 10b), while the near-inertial energy in the mixed layer (KE_I) is largely conserved (Figure 10c).

Figure 10d shows the temporal evolution of each budget term, dKE_I/dt, Π_W, Π_R, and Π_H at 43° S, 93° E. The dKE_I/dt, Π_W, and Π_R terms all have the same order of magnitude, while Π_H term is 1 order of magnitude smaller. The Π_W term is mostly positive, indicating net transfer of energy from the wind into near-inertial currents in the mixed layer. For a given wind event, we first see an increase in Π_W followed by an increase in dKE_I/dt. The dKE_I/dt term rapidly decreases when the increase in Π_W slows down, leading to a peak of dHKE/dt followed by a peak of Π_W 29 hr later (maximum correlation 0.36, $p < 0.95$), about 1.6 times the inertial period at this latitude ($T_f = 17$ hr). Once Π_W starts decreasing, dKE_I/dt changes sign, from positive to negative. The Π_R term is mainly negative, indicating energy loss. Maximum correlation (−0.75, $p < 0.95$) between Π_W and Π_R occurs after 22 hr; this is about 1.2 times the inertial period at this latitude. The energy flux due to change in MLD (Π_H) is negligible.

Over an annual average (Figure 11), Π_W and Π_R balance to leading order. This is not surprising given that dKE_I/dt and Π_H have been reduced by construction in the analysis and Π_R is calculated as a residual. Global maps of Π_W and Π_R present similar spatial patterns, with higher values occurring within the major current systems (Figure 11). Largest values in the Northern Hemisphere correspond to the Kuroshio region and the Gulf Stream. Across each sector of the Southern Ocean, bands of high energy fluxes move southward, from 30° S to 60° S, following the core of the ACC.

Surface kinetic energy fluxes at the near-inertial band decrease by 6% with increasing model resolution (0.16 TW in LLC 1/48° vs. 0.17 TW in LLC 1/24°; see Table 1 and Figure 12). The RMS difference between the two simulations is 30%, with smaller RMS in the 1/48° model. The residual term increases by the same amount, while the rate of change in KE_I and the rate of change in MLD do not change beyond noise level (Figure 12).

4. Discussion

4.1. The Cospectrum of Wind Stress and Ocean Surface Currents

While previous studies have focused on total power input, here we use a frequency-wavenumber cospectrum of wind stress and ocean surface currents to further understand the spatial and temporal scales that combine to give the total flux. The frequency-wavenumber cospectrum of wind stress and ocean surface currents (Figure 2) reveals positive and negative energy inputs to the ocean. The major source of energy to

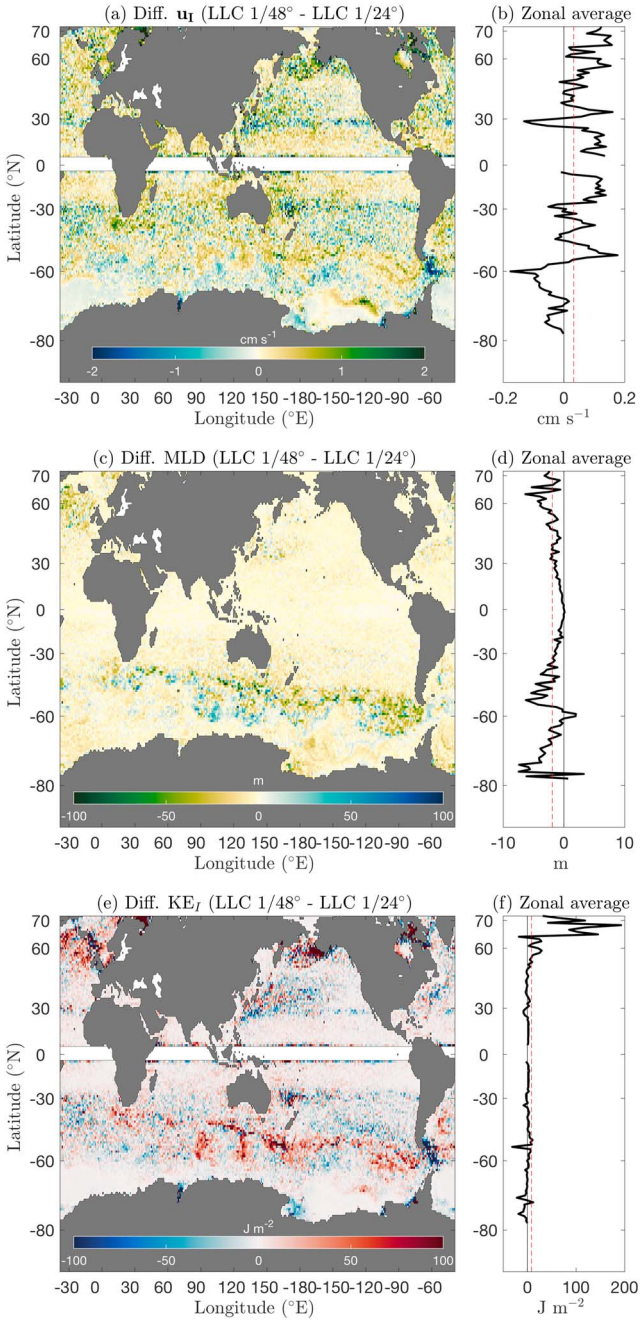

Figure 9. Maps and zonal averages of annual-mean differences (LLC 1/48°-LLC 1/24°) from (a, b) surface near-inertial currents, (c, d) MLD, and (e, f) KE_I. LLC = Latitude-Longitude-polar Cap; MLD = mixed layer depth.

the ocean through the wind work occurs in wintertime in regions with strong synoptic wind variability, that is, Kuroshio Extension and near the Kerguelen Plateau in the Southern Ocean. At large scales (>300 km), positive wind work is found at all frequencies (see the cospectrum in linear form in Figure S2). At the ocean mesoscale and submesoscale, from ~10 to ~300 km and periods from ~12 hr to ~40 days, the cospectrum depicts negative wind energy input.

The impact of tidal frequencies on surface kinetic energy fluxes has not previously been considered. Our results suggest that tidal frequencies are a sink of kinetic energy, and their net negative wind energy input could be explained by the same mechanism that explains the negative energy input at mesoscale. Cospectrum analysis performed using mooring time series (not shown) shows similar results (negative kinetic

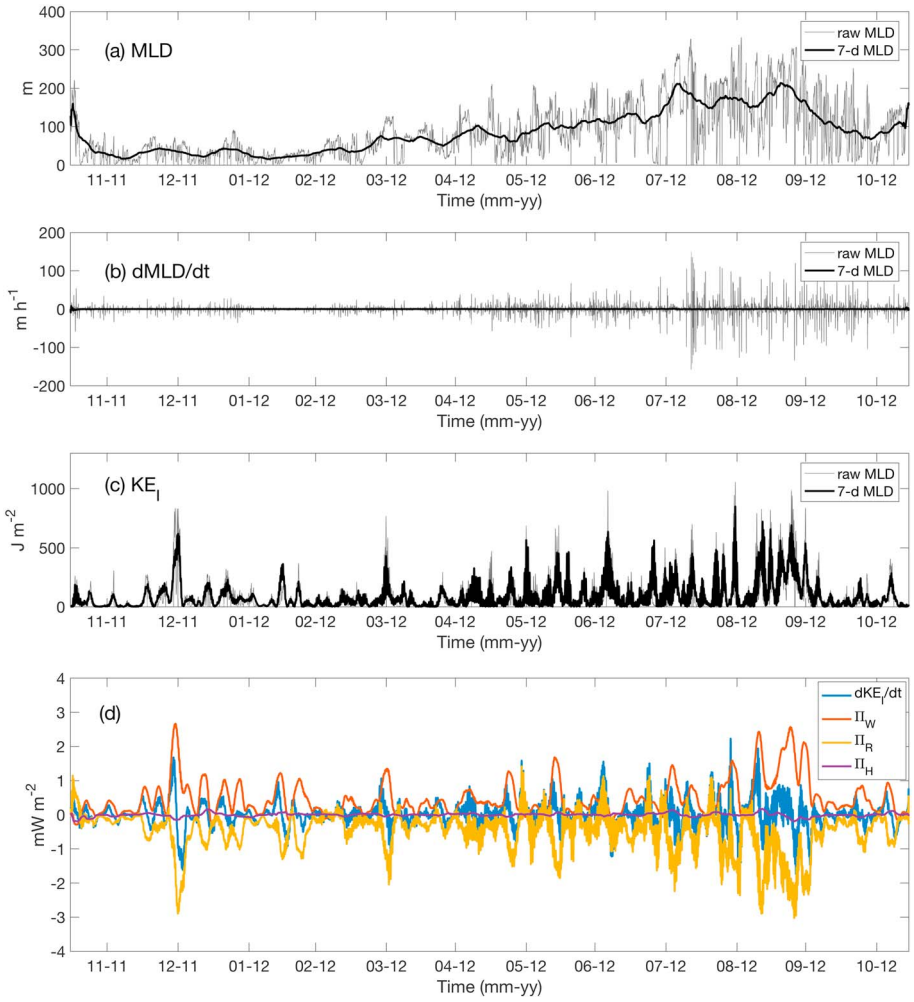

Figure 10. Time series of (a) MLD, (b) rate of change of MLD, and (c) near-inertial energy in the mixed layer (KE_I) East of Kerguelen (43° S, 93° E). Quantities obtained directly from Latitude-Longitude-polar Cap MLD output are shown in light gray (raw), while those obtained from MLD filtered using a 7-day moving average window are shown in black. (d) Near-inertial kinetic energy budget terms: dKE_I/dt (blue), Π_W (red), Π_R (yellow), and Π_H (magenta). MLD = mixed layer depth.

energy fluxes at tidal frequencies). Only semidiurnal tides exhibit significant negative wind work (Figure 2). We hypothesize that this is the effect of baroclinic tides, which are usually observed immediately over the source, or equatorward of the critical latitude. The surface kinetic energy flux calculated in Figure 2 is taken poleward of the critical latitude for diurnal tides (about 30° latitude) and equatorward of the critical latitude of semidiurnal tides (about 74.5° for M2 and 85° for S2). Thus, only surface amplification of the baroclinic tides in the semidiurnal band is expected.

The seasonal variation of upper ocean dynamics (Figure 1c) is captured in the cospectrum of wind stress and ocean surface currents (Figure 2). In wintertime (Figures 2a, 2c, and 2f), a larger synoptic wind variability leads to more energy input into the ocean and to a more energetic mesoscale field, which would lead, consequently, to a larger magnitude of negative surface kinetic energy flux at mesoscales (Table 2). The more energetic IGW field observed in summertime (enhanced negative wind work at frequencies equal and larger than the semidiurnal tides; Figures 2b, 2d, and 2e) could be explained by the intensification of the higher vertical normal modes due to shallower mixed layers (Rocha, Chereskin, et al., 2016).

To examine the impact of spatial resolution in the surface wind and currents fields, a filter transfer function of Gaussian form, $\hat{w} = exp^{-0.5[(k^2\lambda_c^2)-(\omega^2 T_c^2)]}$, is applied to the cospectrum (4). The function considers the cutoff period T_c and the cutoff wavelength λ_c as free parameters. By considering a constant cutoff period of $T_c = 12$ hr, the calculation of the wind work is a function of the resolution. Three cutoff wavelengths λ_c are

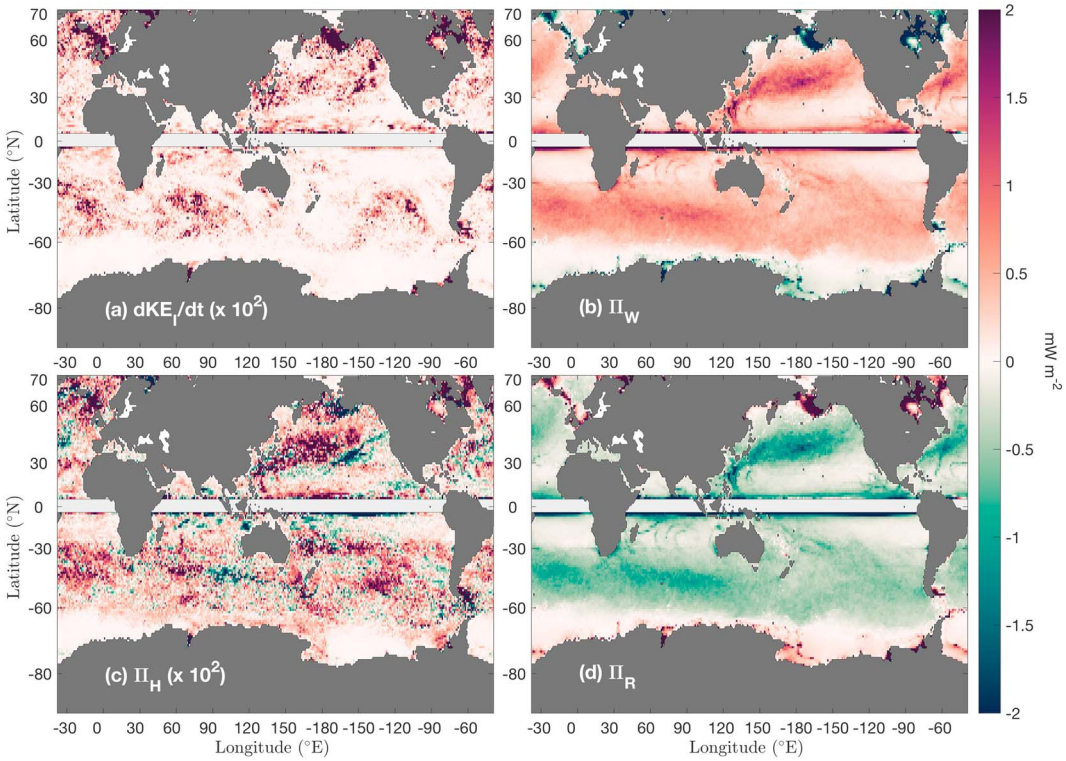

Figure 11. Annual-mean estimates of (a) rate of change in KE_I, (b) Π_W, (c) Π_H, and (d) Π_R (in mW/m^2) calculated from LLC 1/48° hourly wind stress and ocean currents. Note the change in scale: (a) and (c) are two orders of magnitude smaller than (b) and (d).

considered: 200, 100, and 50 km, which is equivalent to having numerical simulations with horizontal resolutions of 100, 50, and 25 km, respectively. To examine the effects of filtering the currents alone, $\hat{w}$ is applied to the surface currents in (4), as $\hat{w}\Lambda_{\tau\mathbf{u}}$. Instead, to examine the effects of filtering both winds and currents, $\hat{w}$ is applied to both winds and currents in (4), leading to $\hat{w}^2\Lambda_{\tau\mathbf{u}}$. When the filter transfer function is applied to surface currents alone, half of the negative surfaces fluxes at mesoscale are contained between 50 and 100 km, and half are between 100 and 200 km (Table 3). Instead, when the filter transfer function is applied to surface currents and winds, 66% of the surface kinetic energy fluxes at mesoscale are contained within 50 to 100 km and 33% within 100 to 200 km. This translates into coarse-resolution simulations (100 km) having unrealistically large total surface kinetic energy flux. As soon as the resolution is large enough to represent mesoscale motions, the wind power input decreases due to the increased drag from the ocean to the atmosphere at such scales.

4.2. Global Surface Kinetic Energy Flux Estimates From LLC

4.2.1. Total Surface Kinetic Energy Flux

Total surface kinetic energy flux estimates from hourly LLC 1/48° are 4.7 TW (Figures 1a and 1c and Table 1). Integrating globally, about half of the contribution comes from time-mean fluxes and the other half from eddy fluxes (Figure 4). Munk and Wunsch (1998) estimated that a total kinetic energy flux of 2.1 TW is needed to maintain the abyssal stratification and the meridional overturning circulation in the ocean. von Storch et al. (2007) estimated that about 30% of the wind input was radiated away from a 114-m-deep layer; applying this consideration to the LLC 1/48° simulation, it would lead to 1.41 TW radiated away from the mixed layer.

The global kinetic energy surface flux value of 4.7 TW is a larger value than previous estimates. For example, von Storch et al. (2007) obtained 3.8 TW using a 1/10° GCM with resting ocean approximation. Wu et al. (2017) used a 1/6° ECCO2 product forced with JRA-55 reanalyis (6-hourly, 55 km; Kobayashi et al., 2015) and obtained 1979–2012 average values of 3.41 TW with resting ocean approximation and 2.55 TW when including ocean surface currents in the wind stress used to calculate wind power input. The latter value represents an 85% increase in LLC's global kinetic energy surface flux values with respect to those obtained from

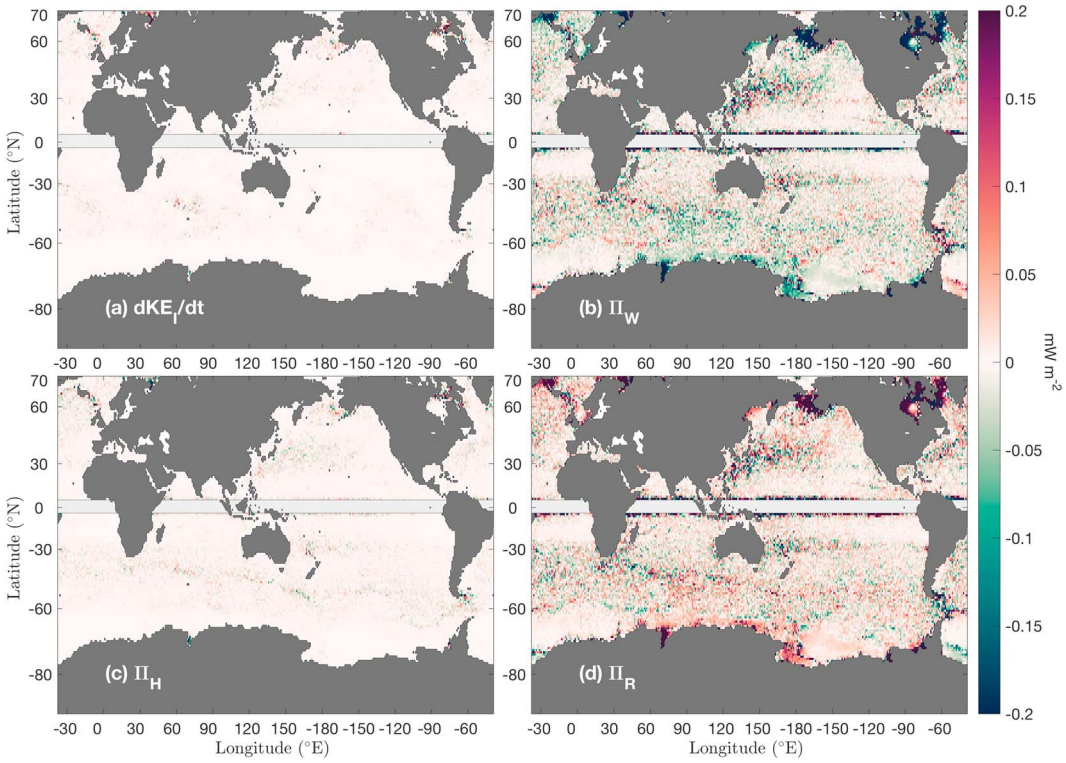

Figure 12. Annual mean of the difference between LLC 1/48° and LLC 1/24° estimates of near-inertial kinetic energy budget terms. (a) Rate of change in KE_I, (b) Π_W, (c) Π_H, and (d) Π_R (in mW/m^2) calculated from hourly wind stress and ocean currents.

the 1/6° ECCO2 product. A number of factors can contribute to this difference, from interannual variability to differences in the reanalysis products. Year 2012 was above the 1979–2012 average wind conditions in JRA-55 reanalysis (Kobayashi et al., 2015). Comparing JRA-55 to ECMWF operational atmospheric forcing conditions for year 2012, the latter shows larger mean wind velocities in the Southern Ocean and larger wind variability in the tropics (not shown). Thus, we attribute LLC's larger kinetic energy fluxes to larger wind variability in 6-hourly mean ECMWF operational wind fields than in the atmospheric forcings used by von Storch et al. (2007) and Wu et al. (2017). Conceivably, future LLC simulations will have even larger surface kinetic energy flux forced by the 1-hourly mean winds from the new generation of EWCWF atmospheric reanalysis (Copernicus Climate Change Service (C3S), 2017).

4.2.2. Near-Inertial Kinetic Energy Fluxes

Fluctuating winds (in space and time) are the main source of near-inertial surface waves. According to different authors, midlatitude winter storms (defined by Zhai, 2017, as "a combination of transient atmospheric phenomena, including synoptic weather systems, cold/warm fronts, and traveling lows that cover a wide range of spatial scale") provide the bulk of near-inertial kinetic energy flux (Alford, 2003; Dippe et al., 2015; Zhai, 2017). The LLC simulations, using ECMWF atmospheric forcing at 15-km horizontal grid resolution, are able to reproduce storm track regions, yet the global wind power input at the near-inertial band (0.16 TW) is low when compared to canonical estimates from slab models, which range between 0.32 and 1.40 TW (Alford, 2001, 2003; Furuichi et al., 2008; Jiang et al., 2011; Watanabe & Hibiya, 2002). We note that the comparison with other model outputs and in situ data is limited by the LLC single-year output. Although slab models do not reproduce the observed kinetic energy balance for strong forcing events because they do not allow for interaction between the mixed layer and the stratified water column below (Plueddemann & Farrar, 2009), they are closest to observations. On the other hand, GCMs provide a more physically realistic representation of the kinetic energy budget with respect to slab models, although they largely underestimate the kinetic energy in the mixed layer, largely due to a combination of too large viscosity and lack of wind variability (Belcher et al., 2012).

Table 3
Surface Kinetic Energy Flux Estimates (in mW/m^2) at Large Scale, Mesoscale, Submesoscale, and IGW After Applying a Gaussian Filter Transfer Function to Wind Stress and Surface Currents and Surface Currents Only to the Kuroshio Cospectrum for JFM and JAS Months

	JFM			JAS		
	200 km	100 km	50 km	200 km	100 km	50 km
Winds and currents						
Large scale	17.0	19.0	20.0	4.0	4.5	4.7
Mesoscale	−0.1	−5.5	−16.6	−0.3	−1.5	−2.9
Submesoscale	−1.6	−4.1	−0.1	−2.4	−1.9	0.0
IGW	0.0	0.0	−0.1	0.0	0.0	−0.1
Total	27.6	23.4	−3.1	3.8	1.9	−2.5
Currents only						
Large scale	24.3	25.6	26.0	5.2	5.5	5.6
Mesoscale	−1.1	−9.9	−21.0	−0.7	−2.1	−3.2
Submesoscale	−2.9	0.0	−0.5	−2.2	0.0	0.0
IGW	−0.2	−0.3	0.4	−0.1	−0.3	−0.6
Total	31.1	21.7	−2.7	3.5	0.6	−3.6

Note. The cutoff period is considered constant (24 hr) and the three cutoff wavelengths considered are 200, 100, and 50 km. See Figure 3 for a schematic of these different regimes in wavenumber/frequency domain. IGW = Internal Gravity Wave.

Previous studies suggest that wind variability on time scales less than 6 hr are critical for accurately representing wind power input. Using a one-dimensional model, Klein et al. (2004) and Klein (2008) estimated a loss of 20% in near-inertial energy when using 6-hourly winds instead of 3-hourly winds. Using a GCM, Rimac et al. (2013) obtained surface near-inertial kinetic energy 3 times higher (up to a factor 4 in the storm track regions) in experiments forced by hourly wind forcing from the National Centers for Environmental Prediction Climate Forecast System Reanalysis (Saha et al., 2010) on 0.35° (about 40 km) resolution grid than in experiments forced by 6-hourly wind stress from the National Centers for Environmental Prediction reanalysis on 1.875° (about 200 km) resolution grid. For 6-hourly winds and 40-km resolution (the closest to the operational ECMWF forcing used in LLC of 6-hourly winds with about 15-km resolution), there is an estimated loss in near-inertial kinetic energy of about 50% at midlatitudes and 70% at high latitudes with respect to 1-hourly wind stress.

Additionally, Rimac et al. (2013) showed the dependence on wind fluctuations in both time and space scales, finding less sensitivity to spatial scale. However, given the minimum horizontal grid resolution considered was 40 km, the role of spatial resolution may have been underestimated. The 85% increase in global wind power in LLC (6-hourly, 15-km atmospheric forcing) with respect to the 1/6°-degree ECCO2 (6-hourly, 55-km atmospheric forcing) suggests that the spatial resolution of atmospheric forcing is also key. Other factors at play may include numerics, dissipation operators, interannual variability, and discrepancies between different reanalysis.

In summary, we attribute the low wind power input at the near-inertial band (Figure 6) and low near-inertial kinetic energy in the mixed layer (Figure 8) obtained with LLC to a combination of factors, which include the use of a GCM (known to underestimate near-inertial motions due to a combination of lack of wind variability and too large viscosity; Belcher et al., 2012) and low wind stress variability (in space and time) in ECMWF forcing.

To obtain an atmospheric wind field that contains enough variability to trigger realistic near-inertial currents is not trivial. Most of the present-day atmospheric reanalysis are based on global meteorological models that successfully reproduce tropospheric winds and permit an accurate representation of large-scale weather patterns. They do not resolve, however, atmospheric boundary layer processes, which occur over scales of only few kilometers and are, in turn, heavily dependent on cloud-resolving processes (Miura et al., 2007). Using cloud-resolving models as atmospheric boundary conditions for ocean circulation models may make possible improving simulations of near-inertial currents.

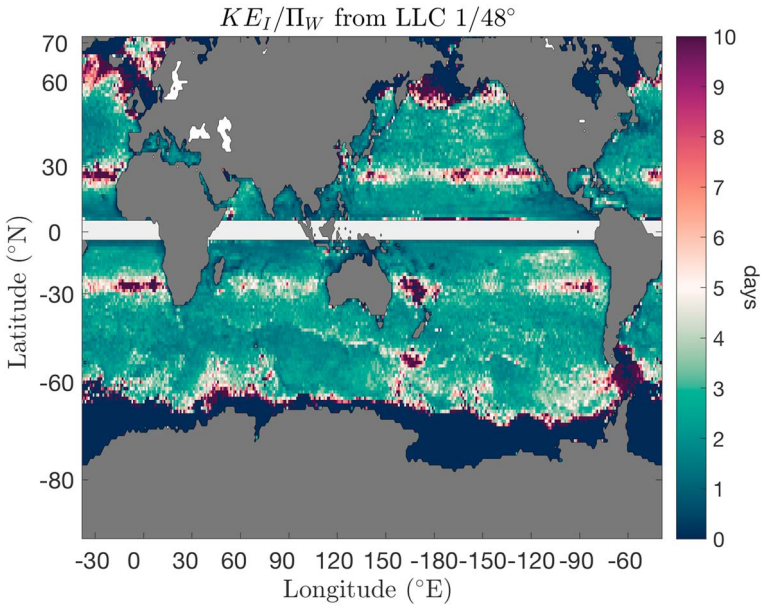

Figure 13. Decay rate, in days, calculated as the ratio between annual-mean estimates of KE_I and Π_W from LLC 1/48°. LLC = Latitude-Longitude-polar Cap.

4.3. On the Near-Inertial Kinetic Energy Budget From LLC Output

We have identified the kinetic energy budget terms in LLC simulations and the values reported (±2 mW/m^2 for dKE_I/dt, Π_W, and Π_R; Figure 10d) are in agreement with previous estimates from mooring data (Majumder et al., 2015) and other numerical estimates (Rath et al., 2014). Here we extend previous works by estimating these budget terms over the global ocean (Figure 11). An annually averaged global map of Π_W presents higher values occurring within the major current systems (Figure 11b), corresponding to Kuroshio region and the Gulf Stream in the Northern Hemisphere and to the core of the ACC in the Southern Ocean.

Most of the variability in the near-inertial kinetic energy flux in the mixed layer ends in the residual term (Figure 11d). The net rate of change of KE_I is small (Figure 11a), which means the kinetic energy budget is almost at equilibrium.

The near-inertial kinetic energy flux, Π_W, is positive (Figure 6 and 11b), and since we are near equilibrium, the residual term is a net sink of mixed layer kinetic energy (i.e., $\Pi_W = -\Pi_R$). Assuming steady state, the simplest way to parameterize this sink of kinetic energy is to use a linear function of the kinetic energy involving a decay rate (D'Asaro, 1985):

$$\Pi_W = -\Pi_R = \frac{r}{2} KE_I, \tag{8}$$

where $r/2$ is the kinetic energy decay rate. In LLC 1/48°, the decay rate of wind-induced near-inertial kinetic energy is about 3 days over most of the global ocean (Figure 13). Particularly slow rates are found in Drake Passage in the Southern Ocean and in the NE Atlantic, as well as along the 30° semidiurnal critical latitude.

The 3-day decay rate of kinetic energy at the near-inertial band found at global scale (Figure 13) lies at the lower bound of other decay rates found in previous works, most of them based on different approaches to the Pollard and Millard (1970) slab model (D'Asaro, 1985). In slab models, r is usually tuned to minimize the difference between modeled and observed $\mathbf{u_I}$, KE_I, or Π_W. Typically, tuned r is in the range of 2–10 days (D'Asaro, 1985; Plueddemann & Farrar, 2009; Pollard & Millard, 1970). These values agree quite well with the decay rates obtained in LLC.

Differences in KE_I between the 1/48° and 1/24° model resolutions (Figures 9e and 9f) arise from a combination of differences in surface inertial currents (Figures 9a and 9b) and of differences in MLD between the two model outputs (Figures 9c and 9d). This is particularly clear in the Southern Ocean, where larger KE_I is found in regions where inertial currents are larger but MLDs are shallower. The key factor affecting KE_I is $|\mathbf{u_I}|$ and not MLD. Surface inertial currents are quadratic in the KE_I expression. The overall reduction in

MLD with increasing resolution is likely related to the model's ability to increasingly resolve submesoscale motions (Su et al., 2018). Restratification of the mixed layer, through mixed layer baroclinic instability, has been shown to cause a reduction in MLD (Belcher et al., 2012; Fox-Kemper et al., 2008, 2011).

5. Conclusion

Improving estimates of surface kinetic energy fluxes is key to understanding the ocean's three-dimensional kinetic energy budget and the processes that support the global overturning circulation. The LLC simulation presents a unique opportunity to recalculate these estimates using submesoscale-permitting, tidal-resolving global ocean output at unprecedented resolution in space and time (~2-km horizontal grid spacing; 90 vertical levels; hourly output). However, steady state in energy balance involves a large number of factors that can all contribute individually, or interact to contribute, to uncertainty. While we expect that new qualitative aspects, like negative work from the tides, to be corroborated by future models and observations, the quantitative predictions may have large uncertainty (not estimated here).

Surface kinetic energy fluxes from LLC simulations lead to 4.71 TW, of which 0.16 TW is at the near-inertial band. A cospectrum analysis of wind stress and ocean surface currents shows positive contribution at large scales and near-inertial frequencies, and negative contribution from mesoscales, tidal frequencies, and IGWs. In general, larger contributions from large scale and mesoscale are observed in winter. The more energetic IGW field is observed in summer. A study on the impact of spatial resolution in the surface wind and currents fields finds that coarse-resolution simulations lead to unrealistically large total surface kinetic energy fluxes. As soon as the model resolution permits to represent mesoscale motions, the wind power input decreases due to the increased drag from the ocean to the atmosphere at such scales.

Surface ocean kinetic energy at the near-inertial band in LLC represents 10% of total surface kinetic energy in the global ocean. Estimates of surface currents and energy content in the mixed layer show qualitatively good agreement with in situ drifter data (spatial patterns are well reproduced; seasonality in mixed layer energy is well reproduced). However, the magnitude of near-inertial currents in LLC is underestimated by a factor of 2, and the near-inertial kinetic energy in the mixed layer in LLC is underestimated by a factor of 2 to 5, when LLC estimates are compared to drifters. The decay rate of near-inertial kinetic energy in the mixed layer from LLC (~2–4 days) is not far from estimates from slab models. We attribute the low values of near-inertial kinetic energy flux, near-inertial surface currents, and near-inertial kinetic energy in the mixed layer obtained with LLC, to a combination of factors, which include the use of a GCM (known to underestimate near-inertial motions), and to limitations in the atmospheric forcing (lack of wind variability, in space and time) used in LLC. We conclude that evaluating the kinetic energy flux from the wind to ocean inertial motions should include time-varying winds and surface currents, time-dependent MLD estimates, and high spatial resolutions that permit solving for submesoscale processes.

Appendix A: Explanation of the Negative Cospectrum at Mesoscales

The cospectrum of wind stress and ocean surface currents depicts negative values in the mesoscale and submesoscale regime, ranging wavelengths from ~10 to ~300 km and periods from ~12 hr to ~40 days. The energy flux continuously spread out in this region of the cospectrum is associated with mesoscale and submesoscale balanced motions (Rocha, Chereskin, et al., 2016; Qiu et al., 2017). In order to explain the negative wind work, we invoke two formulations to compute the wind stress: the bulk formula described in equation (1), $\boldsymbol{\tau} = \rho_{\text{air}} C_d \left|\mathbf{U_{10}} - \mathbf{u}\right| \left(\mathbf{U_{10}} - \mathbf{u}\right)$, and the standard equation to compute the wind stress without taking into account the ocean surface currents, $\boldsymbol{\tau}_{\text{std}} = \rho_{\text{air}} C_d \left|\mathbf{U_{10}}\right| \left(\mathbf{U_{10}}\right)$. Now the wind work difference due to the formulations of τ is (assuming $\mathbf{u}$ the same in both cases)

$$\rho_0 \left(\boldsymbol{\tau} \cdot \mathbf{u} - \boldsymbol{\tau}_{\text{std}} \cdot \mathbf{u}\right) = -\rho_{\text{air}} C_d \left|\mathbf{U_{10}} - \mathbf{u}\right| |\mathbf{u}|^2 - \rho_{\text{air}} C_d \left(\left|\mathbf{U_{10}}\right| - \left|\mathbf{U_{10}} - \mathbf{u}\right|\right) \mathbf{U_{10}} \cdot \mathbf{u}. \tag{A1}$$

Since surface winds are usually at least an order of magnitude faster than surface currents, in such a way that $\left|\mathbf{U_{10}} - \mathbf{u}\right| \sim \left|\mathbf{U_{10}}\right|$, therefore, the difference in the wind work between both formulation reduces to the leading order

$$\rho_0 \left(\boldsymbol{\tau} \cdot \mathbf{u} - \boldsymbol{\tau}_{\text{std}} \cdot \mathbf{u}\right) \sim -\rho_{\text{air}} C_d \left|\mathbf{U_{10}}\right| |\mathbf{u}|^2. \tag{A2}$$

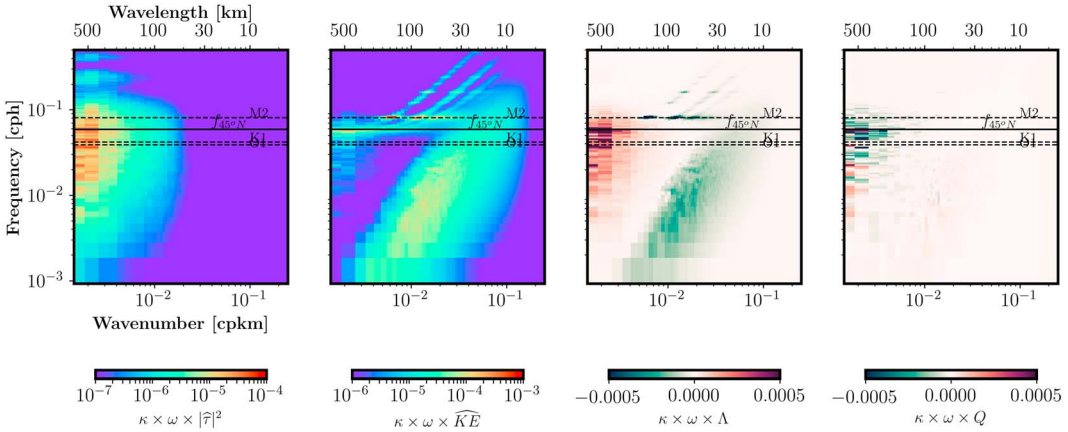

Figure B1. Frequency-wavenumber spectrum for wind stress (first panel), kinetic energy (second panel), cospectrum of wind stress and ocean surface currents (third panel), and quadrature spectrum of wind stress and ocean surface currents (fourth panel).

Note the negative nature of the expression, meaning that the wind stress formulation involving the feedback from the surface ocean currents is to remove energy, that is, to apply a surface drag on the circulation (Eden & Dietze, 2009).

Appendix B: Error Estimation in Cospectral Analysis

The normalized random error associated to the cospectral analysis was estimated following the formula described in Bendat and Piersol (2000, p. 321):

$$\epsilon[\Lambda(\kappa_r,\omega)] = \frac{[G_{xx}G_{yy} + \Lambda^2(\kappa_r,\omega) - Q(\kappa_r,\omega)]^{1/2}}{|\Lambda(\kappa_r,\omega)|\sqrt{2n_d}}. \tag{B1}$$

Adapting equation (B1) to our surface kinetic energy flux spectral analysis, $G_{xx}(\kappa_r,\omega)$ is the frequency-wavenumber spectrum of wind stress, $G_{yy}(\kappa_r,\omega)$ is the frequency-wavenumber spectrum of ocean currents, $\Lambda(\kappa_r,\omega)$, is the frequency-wavenumber cospectrum (in-phase signal) of wind stress and ocean surface currents, $Q(\kappa_r,\omega)$ is the frequency-wavenumber quadrature spectrum (out-phase signal) of wind stress and ocean surface currents (note that $\Lambda^2 - Q^2$), and n_d is the number of contiguous segments in which the time series is broken. In our case, the time series was divided into two segments of 90 days. Note that ϵ varies inversely with n_d. These four quantities involved in the quantification of the random error are displayed in Figure B1 for the winter season JFM in the Kuroshio region.

The RMS error can be estimated by multiplying the normalized random error ϵ by the true value ϕ (RMS error $= \epsilon|\phi|$; Bendat & Piersol, 2000, p. 23, Equation 1.18). Approximating the true value ϕ with the cospectrum $|\Lambda|$, the expression to compute RMS error is $\epsilon|\Lambda|$. As expected, the RMS error varies as a function of frequency and wavenumber (Figure B2). Its distribution resembles the cospectrum, and the RMS error is 1 order of magnitude smaller than the cospectrum. Figure B2 displays the largest errors (± 2 W/m^2 / [cph × cpkm]) at wavelengths greater than 500 km and an additional peak between 100 and 250 km at lower frequencies.

The RMS error in the different spectral bands (large scale, mesoscale, inertial, semidiurnal, and IGWs, defined in Figure 3) is

$$RMS_{error}(\kappa_1 > \kappa > \kappa_2, \omega_1 > \omega > \omega_2) = \int_{\kappa_1}^{\kappa_2}\int_{\omega_1}^{\omega_2} \epsilon[\Lambda(\kappa_r,\omega)]|\Lambda(\kappa_r,\omega)|d\kappa d\omega, \tag{B2}$$

where $d\kappa$ is the spacing of the discrete wavenumbers; $d\omega$ is the spacing of the discrete frequencies; and κ_1, κ_2, ω_1, and ω_2 are the bounds of the spectral bands. The RMS error for each spectral band during JFM and JAS seasons in the Kuroshio region are given in Table 2.

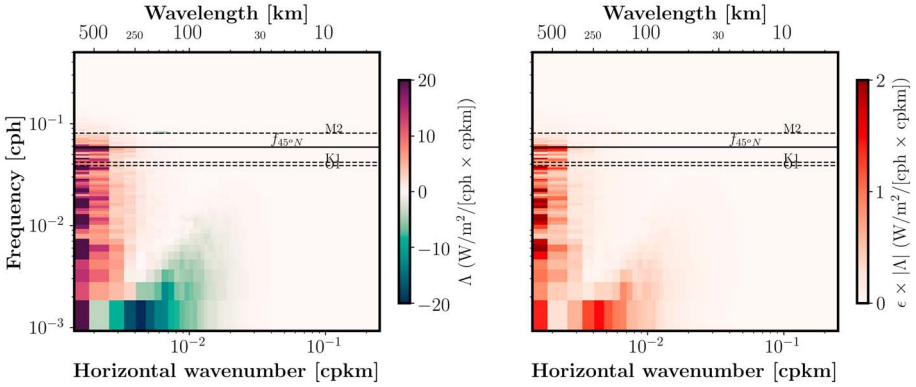

Figure B2. Frequency-wavenumber cospectrum of wind stress and ocean surface currents (left) and Root-Mean-Square error for the cospectrum (right).

Acknowledgments
We thank three anonymous reviewers for their helpful comments that led to an improved manuscript. We are grateful to Jörn Callies and Laurie Padman for fruitful discussions. This work is funded by the National Aeronautics and Space Administration (NASA) through the project "Towards improved estimates of upper ocean energetics: Science motivation for the simultaneous measurement of ocean surface vector winds and currents" (Grant NNX15AG42G) and through NASA Grant NNX14AM71G and NNX16AH76G. Model output from global 1/48° and 1/24° ECCO2 MITgcm simulations is freely available to the community. For access of the full solutions, we recommend that users apply for an HEC account at NASA Ames. Data are provided online (~dmenemen/llc/). Users without a NASA Ames account may explore what is available online (https://data.nas.nasa.gov/ecco/). This work was, in part, performed at the Jet Propulsion Laboratory, California Institute of Technology, under contract with the National Aeronautics and Space Administration. Color maps used in this contribution are from Thyng et al. (2016). To Teresa and Francesc, for their patience.

References

Adcroft, A., Hill, C., & Marshall, J. A. (1997). Representation of topography by shaved cells in a height coordinate ocean model. *Monthly Weather Review*, *125*, 2293–2315.

Alford, M. H. (2001). Internal swell generation: The spatial distribution of energy flux from the wind to mixed layer near-inertial motions. *Journal of Physical Oceanography*, *31*, 2359–2368.

Alford, M. H. (2003). Improved global maps and 54-year history of wind-work on ocean inertial motions. *Geophysical Research Letters*, *30*(8), 1424. https://doi.org/10.1029/2002GL016614

Arbic, B. K., Alford, M. H., Ansong, J. K., Buijsman, M. C., Ciotti, R. B., Farrar, J. T., et al. (2018). A primer on global internal tide and internal gravity wave continuum modeling in HYCOM and MITgcm. In J. T. E. Chassignet, A. Pascual, & E. J. Verron (Eds.), *New frontiers in operational oceanography* pp. 307–392: GODAE OceanView. https://doi.org/10.17125/gov2018.ch13

Arbic, B. K., Wallcraft, A. J., & Metzger, E. J. (2010). Concurrent simulation of the eddying general circulation and tides in a global ocean model. *Ocean Modelling*, *32*, 175–187. https://doi.org/10.1016/j.ocemod.2010.01.007

Belcher, S. E., Grant, A. L. M., Hanley, K. E., Fox-Kemper, B., Roekel, L. V., Sullivan, P. P., et al. (2012). A global perspective on Langmuir turbulence in the ocean surface boundary layer. *Geophysical Research Letters*, *39*, L18605. https://doi.org/10.1029/2012GL052932

Bendat, J. S., & Piersol, A. G. (2000). *Random data: Analysis and measurements procedures* (3rd ed.)., pp. 594. New York, NY: Wiley-Interscience.

Chaigneau, A., Pizarro, O., & Rojas, W. (2008). Global climatology of near-inertial current characteristics from Lagrangian observations. *Geophysical Research Letters*, *35*, L13603. https://doi.org/10.1029/2008GL034060

Copernicus Climate Change Service (C3S) (2017). ERA5: Fifth generation of ECMWF atmospheric reanalyses of the global climate. Copernicus Climate Change Service Climate Data Store (CDS) https://cds.climate.copernicus.eu

D'Asaro, E. (1985). The energy flux from the wind to near-inertial motions in the surface mixed layer. *Journal of Physical Oceanography*, *15*, 1043–1059. https://doi.org/10.1175/1520-0485

Daru, V., & Tenaud, C. (2004). High order one-step monotonicity-preserving schemes for unsteady compressible flow calculations. *Journal of Computational Physics*, *193*, 563–594.

Dawe, J. T., & Thompson, L. (2006). Effect of ocean surface currents on wind stress, heat flux, and wind power input to the ocean. *Geophysical Research Letters*, *33*, L09604. https://doi.org/10.1029/2006GL025784

De Boyer Montegut, C., Madec, G., Fischer, A. S., Lazar, A., & Iudicone, D. (2004). Mixed layer depth over the global ocean: An examination of profile data and a profile-based climatology. *Journal of Geophysical Research*, *109*, C12003. https://doi.org/10.1029/2004JC002378

Dippe, T., Zhai, X., Greatbatch, R. J., & Rath, W. (2015). Interannual variability of wind power input to near-inertial motions in the North Atlantic. *Ocean Dynamics*, *65*, 859–875.

Dong, S., Sprintall, J., Gille, S. T., & Talley, L. (2008). Southern Ocean mixed-layer depth from Argo float profiles. *Journal of Geophysical Research*, *113*, C06013. https://doi.org/10.1029/2006JC004051

Duhaut, T. H. A., & Straub, D. N. (2006). Wind stress dependence on ocean surface velocity: Implications for mechanical energy input to ocean circulation. *Journal of Physical Oceanography*, *36*, 202–211.

ETOPO-5 (1988). Data Announcement 88-MGG-02, *Digital relief of the surface of the Earth*. Boulder, Colorado: NOAA, National Geophysical Data Center.

Eden, C., & Dietze, H. (2009). Effects of mesoscale eddy/wind interactions on biological new production and eddy kinetic energy. *Journal of Geophysical Research*, *114*, C05023. https://doi.org/10.1029/2008JC005129

Elipot, S., & Gille, S. T. (2009). Estimates of wind energy input to the Ekman layer in the Southern Ocean from surface drifter data. *Journal of Geophysical Research*, *114*, C06003. https://doi.org/10.1029/2008JC005170

Elipot, S., & Lumpkin, R. (2008). Spectral description of oceanic near-surface variability. *Geophysical Research Letters*, *35*, L05606. https://doi.org/10.1029/2007GL032874

Elipot, S., Lumpkin, R., Perez, R. C., Lilly, J. M., Early, J. J., & Sykulski, A. M. (2016). A global surface drifter data set at hourly resolution. *Journal of Geophysical Research: Oceans*, *121*, 2937–2966. https://doi.org/10.1002/2016JC011716

European Centre for Medium-Range Weather Forecasts (2011). ECMWF's operational model analysis, starting in 2011, *Research data archive at the National Center for Atmospheric Research*. Boulder,Colorado: Computational and Information Systems Laboratory. https://doi.org/10.5065/D6ZG6Q9F

Ferrari, R., & Wunsch, C. (2009). Ocean circulation kinetic energy: Reservoirs, sources, and sinks. *Annual Review of Fluid Mechanics*, *41*, 253–282.

Fox-Kemper, B., Danabasoglu, G., Ferrari, R., Griffies, S. M., Hallberg, R. W., Holland, M. M., et al. (2011). Parameterization of mixed layer eddies. Part III: Implementation and impact in global ocean climate simulations. *Ocean Modelling*, *39*, 61–78.

Fox-Kemper, B., Ferrari, R., & Hallberg, R. (2008). Parameterization of mixed layer eddies. Part I: Theory and diagnosis. *Journal of Physical Oceanography*, *38*(6), 1145–1165.

Fox-Kemper, B., & Menemenlis, D. (2008). Can large eddy simulation techniques improve mesoscale rich ocean models? In B. Fox-Kemper, & D. Menemenlis (Eds.), *Ocean modeling in an eddying regime* pp. 319–338). Washington, D. C.: Amer. Geophys. Union.

Fu, L. L. (1981). Observations and models of inertial waves in the deep ocean. *Reviews of Geophysics and Space Physics*, *19*, 141–170.

Furuichi, N., Hibiya, T., & Niwa, Y. (2008). Model-predicted distribution of wind-induced internal wave energy in the world's oceans. *Journal of Geophysical Research*, *113*, C09034. https://doi.org/10.1029/2008JC004768

Gille, S. T. (2005). Statistical characterization of zonal and meridonal ocean wind stress. *Journal of Atmospheric and Oceanic Technology*, *22*, 1353–1372.

Hasselmann, K. (1970). Wave-driven inertial oscillations. *Geophysical Fluid Dynamics*, *1*, 463–502.

Hill, C., Menemenlis, D., Ciotti, B., & Henze, C. (2007). Investigating solution convergence in a global ocean model using a 2048-processor cluster of distributed shared memory machines. *Scientific Programming*, *15*, 107–115.

Huang, R. X. (2004). Energy flows in the ocean. In R. X. Huang (Ed.), *Encyclopedia of energy* pp. 497–509): Elsevier.

Hughes, C. W., & Wilson, C. (2008). Wind work on the geostrophic ocean circulation: An observational study of the effect of small scales in the wind stress. *Journal of Geophysical Research*, *113*, C02016. https://doi.org/10.1029/2007JC004371

Jiang, J., Lu, Y., & Perrie, W. (2011). Estimating the energy flux from the wind to ocean inertial motions: The sensitivity to surface wind fields. *Geophysical Research Letters*, *32*, L15610. https://doi.org/10.1029/2005GL023289

Klein, P. (2008). High-frequency winds and eddy resolving models. In M. W. Hecht, & H. Hasumi (Eds.), *Ocean modeling in an eddying regime* pp. 83–100). Washington, D. C: American Geophysical Union. https://doi.org/10.1029/177GM07

Klein, P., Lapeyre, G., & Large, W. G. (2004). Wind ringing of the ocean in presence of mesoscale eddies. *Geophysical Research Letters*, *31*, L15306. https://doi.org/10.1029/2004GL020274

Kobayashi, S., Ota, Y., Harada, Y., Ebita, A., Moriya, M., Onoda, H., et al. (2015). The JRA-55 Reanalysis: General specifications and basic characteristics. *Journal of the Meteorological Society of Japan*, *93*, 5–48. https://doi.org/10.2151/jmsj.2015-001

Kundu, P. K. (1976). An analysis of inertial oscillations observed near Oregon coast. *Journal of Physical Oceanography*, *6*, 879–893.

Large, W. G., McWilliams, J. C., & Doney, S. C. (1994). Oceanic vertical mixing: A review and a model with a nonlocal boundary layer parameterization. *Reviews of Geophysics*, *32*, 363–403.

Large, W. G., & Pond, S. (1982). Sensible and latent heat flux measurements over the ocean. *Journal of Physical Oceanography*, *12*, 464–482.

Large, W. G., & Yeager, S. G. (2004). Diurnal to decadal global forcing for ocean and sea-ice models: The data sets and flux climatologies, *NCAR Tech. Note NCAR/TN-460+STR* pp. 105). Boulder, Colo. Natl. Cent. for Atmos. Res.

Losch, M., Menemenlis, D., Campin, J.-M., Heimback, P., & Hill, C. (2010). On the formulation of sea-ice models. Part 1: Effects of different solver implementations and parameterizations. *Ocean Modelling*, *33*, 129–144.

MacKinnon, J. A., Alford, M. H., Bouruet-Aubertot, P., Bindoff, N., Gille, S., Girton, J. B., et al. (2010). Using global arrays to investigate internal waves and mixing. In J. Hall, D. E. Harrison, & D. Stammer (Eds.), *Proceedings of OceanObs'09: Sustained ocean observations and information for society* (Vol. 2, pp. 58). Venice, Italy: ESA Publication WPP-306. https://doi.org/10.5270/OceanObs09.cwp.58

Majumder, S., Tandon, A., Rudnick, D. L., & Farrar, J. T. (2015). Near-inertial kinetic energy budget of the mixed layer and shear evolution in the transition layer in the Arabian Sea during the monsoons. *Journal of Geophysical Research: Oceans*, *120*, 6492–6507. https://doi.org/10.1002/2014JC010198

Marshall, J. A., Adcroft, A., Hill, C., Perelman, L., & Heisey, C. (1997). A finite-volume, incompressible Navier-Stokes model for studies of the ocean on parallel computers. *Journal of Geophysical Research*, *102*, 5753–5766.

McWilliams, J. C., & Restrepo, J. M. (1999). The wave-driven ocean circulation. *Journal of Physical Oceanography*, *29*, 2523–2540.

Menemenlis, D., Campin, J., Heimbach, P., Hill, C., Lee, T., Nguyen, A., et al. (2008). ECCO2: High resolution global ocean and sea ice data synthesis. *Mercator Ocean Quarterly Newsletter*, *31*, 13–21.

Milliff, R. F., Morzel, J., Chelton, D. B., & Freilich, M. H. (2004). Wind stress curl and wind stress divergence biases from rain effects on QSCAT surface wind retrievals. *Journal of Atmospheric and Oceanic Technology*, *21*, 1216–1231.

Miura, H., Satoh, M., Nasuno, T., Noda, A. T., & Oouchi, K. (2007). A Madden-Julian Oscillation event realistically simulated by a global cloud-resolving model. *Science*, *318*, 1763–1765.

Munk, W., & Phillips, N. (1968). Coherence and band structure of inertial motion in the sea. *Reviews of Geophysics*, *6*(12), 447–472.

Munk, W., & Wunsch, C. (1998). Abyssal recipes II: Energetics of tidal and wind mixing. *Deep Sea Research*, *45*(12), 1977–2010.

Plueddemann, A. J., & Farrar, J. T. (2009). Observations and models of the energy flux from the wind to mixed-layer inertial currents. *Deep Sea Research II*, *53*, 5–30.

Pollard, R., & Millard, R. (1970). Comparison between observed and simulated wind-generated inertial oscillations. *Deep Sea Research*, *17*, 153–175.

Qiu, B., Nakano, T., Chen, S., & Klein, P. (2017). Submesoscale transition from geostrophic flows to internal waves in the northwestern Pacific upper ocean. *Nature Communications*, *8*, 14055. https://doi.org/10.1038/ncomms14055

Rascle, N., Ardhuin, F., Queffeulou, P., & Croizé-Fillon, D. (2008). A global wave parameter database for geophysical applications. Part 1: Wave–current-turbulence interaction parameters for the open ocean based on traditional parameterizations. *Ocean Modelling*, *25*, 154–171.

Rath, W., Greatbatch, R. J., & Zhai, X. (2013). Reduction of near-inertial energy through the dependence of wind stress on the ocean-surface velocity. *Journal of Geophysical Research: Oceans*, *118*, 2761–2773. https://doi.org/0.1002/jgrc.20198

Rath, W., Greatbatch, R. J., & Zhai, X. (2014). On the spatial and temporal distribution of near-inertial energy in the Southern Ocean. *Journal of Geophysical Research: Oceans*, *119*, 359–376. https://doi.org/10.1002/2013JC009246

Rimac, A., von J.-S., Storch, C. Eden, & Haak, H. (2013). The influence of high-resolution wind stress field on the power input to near-inertial motions in the ocean. *Geophysical Research Letters*, *40*, 4882–4886. https://doi.org/10.1002/grl.50929

Rocha, C. B., Chereskin, T. K., Gille, S. T., & Menemenlis, D. (2016). Mesoscale to submesoscale wavenumber spectra in Drake Passage. *Journal of Physical Oceanography*, *46*(2), 601–620.

Rocha, C. B., Gille, S. T., Chereskin, T. K., & Menemenlis, D. (2016). Seasonality of submesoscale dynamics in the Kuroshio Extension. *Geophysical Research Letters*, *43*, 11,304–11,311. https://doi.org/10.1002/2016GL071349

Saha, S., Moorthi, S., Pan, H.-L., Wu, X., Wang, J., Nadiga, S., et al. (2010). The NCEP Climate Forecast System Reanalysis. *Bulletin of the American Meteorological Society*, *91*, 1015–1057. https://doi.org/10.1175/2010BAMS3001.1

Savage, A. C., Arbic, B. K., Alford, M. H., Ansong, J. K., Farrar, J. T., Menemenlis, D., et al. (2017). Spectral decomposition of internal gravity wave sea surface height in global models. *Journal of Geophysical Research: Oceans*, *122*, 7803–7821. https://doi.org/10.1002/2017JC013009

Savage, A. C., Arbic, B. K., Richman, J. G., Shriver, J. F., Alford, M. H., Buijsman, M. C., et al. (2017). Frequency content of sea surface height variability from internal gravity waves to mesoscale eddies. *Journal of Geophysical Research: Oceans*, *122*, 2519–2538. https://doi.org/10.1002/2016JC012331

Simmons, A. J., & Gibson, J. K. (2000). The ERA-40 project plan, *ERA-40 Proj. Rep. Ser. 1* pp. 62). United Kingdom: Eur. Cent. for Medium-range Weather Forecasts Reading.

Su, Z., Wang, J., Klein, P., Thompson, A. F., & Menemenlis, D. (2018). Ocean submesoscales as a key component of the global heat budget. *Nature Communications*, *9*, 775. https://doi.org/10.1038/s41467-018-02983-w

Thompson, A. F., Lazar, A., Buckingham, C., Garabato, A. C. N., Damerell, G. M., & Heywood, K. J. (2016). Open-ocean submesoscale motions: A full seasonal cycle of mixed layer instabilities from gliders. *Journal of Physical Oceanography*, *46*(4), 1285–1307.

Thyng, K., Greene, C., Hetland, R., Zimmerle, H., & DiMarco, S. (2016). True colors of oceanography: Guidelines for effective and accurate colormap selection. *Oceanography*, *29*(3), 9–13.

von Storch, J.-S., Sasaki, H., & Marotzke, J. (2007). Wind-generated power input to the deep ocean: An estimate using a 1/10° general circulation model. *Journal of Physical Oceanography*, *37*, 657–672.

Wang, W., & Huang, R. X. (2004). Wind energy input to the surface waves. *Journal of Physical Oceanography*, *34*, 1276–1280.

Watanabe, M., & Hibiya, T. (2002). Global estimates of the wind-induced energy flux to inertial motions in the surface mixed layer. *Geophysical Research Letters*, *29*(8), 1239. https://doi.org/10.1029/2001GL014422

Wu, Y., Zhai, X., & Wang, X. (2017). Decadal-mean impact of including ocean surface currents in bulk formulas on surface airsea fluxes and ocean general circulation. *Journal of Climate*, *30*, 9511–9525. https://doi.org/10.1175/JCLI-D-17-0001.1

Wunsch, C. (1998). The work done by the wind on the oceanic general circulation. *Journal of Physical Oceanography*, *28*, 2331–2339.

Wunsch, C., & Ferrari, R. (2004). Vertical mixing, energy, and the general circulation of the oceans. *Annual Review of Fluid Mechanics*, *36*, 281–314.

Zhai, X. (2013). On the wind mechanical forcing of the ocean general circulation. *Journal of Geophysical Research: Oceans*, *118*, 6561–6577. https://doi.org/10.1002/2013JC009086

Zhai, X. (2017). Dependence of energy flux from the wind to surface inertial currents on the scale of atmospheric motions. *Journal of Physical Oceanography*, *47*, 2711–2719.

Zhai, X., Greatbatch, R., Eden, C., & Hibiya, T. (2009). On the loss of wind-induced near-inertial energy to turbulent mixing in the upper ocean. *Journal of Physical Oceanography*, *39*, 3040–3045.

Zhai, X., Johnson, H. L., Marshall, D. P., & Wunsch, C. (2012). On the wind power input to the ocean general circulation. *Journal of Physical Oceanography*, *42*, 1357–1365.

Zhai, X., & Wunsch, C. (2013). On the variability of wind power input to the oceans with a focus on the subpolar North Atlantic. *Journal of Climate*, *26*, 3892–3903.